Winter 12-14-2018

MINERALOGY, PETROLOGY, AND GEOCHEMISTRY OF THE UNIQUE SILICA-RICH UNGROUPED ACHONDRITE NORTHWEST AFRICA 11575

Mya Ann Habermann
University of New Mexico

Mya Habermann

Candidate

Earth and Planetary Sciences Department

Department

This thesis is approved, and it is acceptable in quality and form for publication:

Approved by the Thesis Committee:

Dr. Carl Agee , Chairperson

Dr. Jin Zhang

Dr. Karen Ziegler

Dr. Zachary Sharp

Mineralogy, Petrology, and Geochemistry of the Unique Silica-rich Ungrouped Achondrite Northwest Africa 11575

BY

MYA A. HABERMANN

B.S., Geology, University of Georgia, 2015

THESIS

Submitted in Partial Fulfillment of the

Requirements for the Degree of

Master of Science

Earth and Planetary Sciences

The University of New Mexico

Albuquerque, New Mexico

May, 2019

Acknowledgements

I am immensely grateful for the support and encouragement I have received from friends, colleagues, professors, and family while I have sought to further my education.

I would like to thank my current advisor, Dr. Carl Agee, for his support and guidance on this project. My committee members, Dr. Karen Ziegler, Dr. Zachary Sharp, and Dr. Jin Zhang, for their suggestions, wealth of knowledge, and support throughout the last two years.

This research could not have been possible without those who helped with instrumentation or contributed directly to the research and this manuscript. Thank you to Dr. Mike Spilde for his training and assistance with the microprobe. Thank you to Dr. Karen Ziegler for contributing the oxygen isotopic analyses, and to Dr. Qing-Zhu Yin and Dr. Matthew Sanborn for providing the chromium isotopic analyses and the methods section detailing the Chromium isotope measurements. Thank you to Dr. Francis McCubbin and Dr. Jessica Barnes for performing the NanoSIMS and EPMA analyses on the apatite and merrillite, and for contributing the methods sections for the nanoSIMS and the portion of the EPMA methods pertaining to the apatite and merrillite analyses. Thank you to Eric Peterson for performing the XRD analysis. Thank you to Dr. Chip Shearer, and Dr. Adrian Brearley for helping me with data interpretation, and to Dr. Gary Weissmann for his support and exciting TA positions.

Thank you to Shannon Clark, Beth Ha, Cindy Jaramillo, Faith Mutchnik, Paula Pascetti, and Mabel Chavez for their constant help and support.

This work was supported by Dr. Carl Agee's NASA grants, numbers NNX14AK43G and NNX14AI23G, and the New Mexico Space Grant.

MINERALOGY, PETROLOGY, AND GEOCHEMISTRY OF THE UNIQUE SILICA-RICH UNGROUPED ACHONDRITE NORTHWEST AFRICA 11575

By

Mya A. Habermann

B.S., Geology, University of Georgia, 2015

M.S. Earth and Planetary Sciences, University of New Mexico, 2019

ABSTRACT

We report here on a unique, newly discovered, silica-rich ungrouped achondrite Northwest Africa 11575 (NWA 11575). NWA 11575 is one of four known silica-rich ungrouped achondrites, presenting evidence for igneous processes resulting in evolved compositions early in the history of the solar system. It is unique from the other silica-rich ungrouped achondrites in that it has pyroxene compositional trends matching those of lunar samples and martian meteorites; contains quartz and potassium feldspar; and contains oxygen, hydrogen, and chromium isotopes that are similar to those of LL chondrites. Together, these four silica-rich ungrouped achondrites provide evidence for evolved compositions resulting from igneous processes on at least three separate bodies.

NWA 11575 consists of two lithologies, the host or light lithology and the dark lithology. The dark lithology occurs as clasts within the light lithology, with a distinct contact between the lithologies. The mineralogy of the host lithology consists of 53.8% oligoclase, 34.1% pyroxene, 4.8% potassium feldspar, 3.8% quartz, and 2.6% apatite and merrillite, along with minor chromite, ilmenite, iron oxide, iron sulfide, and low-Ni iron.

The apatite is three times more abundant than the merrillite. The dark lithology consists of 70% groundmass and 30% pyroxenes but has a similar trachyandesitic to andesitic bulk composition. Apatite is present in some regions within the dark lithology but is not ubiquitous. The pyroxene compositional zoning trend for the light lithology consists of magnesian pigeonite, mantled by an augitic layer, and then rimmed by ferropigeonite. Numerous similarities between the host and dark lithologies, such as similar oxygen isotopic compositions, bulk compositions, and pyroxene trends, suggest that the host and dark lithology are derived from the same source, but differ in their cooling and crystallization histories.

One possible interpretation is that the host and dark lithologies are lavas formed through extensive magmatic differentiation, possibly derived from a precursor of chondritic composition, which erupted on the surface of their parent body. The dark lithology cooled quickly forming a quenched glass with hopper pyroxenes. The later-erupted material, perhaps with more overlying material to insulate the magma and provide for a slower cooling rate, cooled slowly enough to crystallize complexly zoned pyroxenes, feldspars, and a residual mesostasis of quartz, potassium feldspar, apatite, and minor phases. Alternatively, the dark lithology could be an impact melt. Either process could have occurred on a volcanic parent body with oxygen isotopes similar to those of LL chondrites, or at some location on the LL-chondrite parent body itself.

TABLE OF CONTENTS

LIST OF FIGURES

LIST OF TABLES

1.0 Introduction

Northwest Africa 11575 (NWA 11575) is classified as an ungrouped achondrite, because it is 1) higher in bulk SiO_2 content than any other group of meteorites, 2) isotopically similar to ordinary chondrites, but displays clear igneous textures precluding it from being considered a chondrite, and 3) contains complex pyroxene zoning trends similar to martian and lunar samples. Three other silica-rich ungrouped achondrites have been studied, NWA 11119, Alma-A, and GRA 06128/9. The silica-rich ungrouped achondrites vary in their oxygen isotopic composition and have varying amounts of silica and alkalis, suggesting that they formed on different parent bodies. Furthermore, the crystallization ages of NWA 11119, Alma-A, and GRA 06128/9 are all between 4.568 and 4.526 Ga, suggesting that igneous processes were producing silica-rich compositions (greater than 55 wt% SiO_2) early in the history of the solar system. NWA 11575 is unique from the other ungrouped achondrites because it has a pyroxene zoning trend matching that of lunar and martian pyroxenes, contains quartz and potassium feldspar, and has an oxygen isotopic composition that is similar to that of LL chondrites.

Northwest Africa 11119 (NWA 11119) is the most recently found of these felsic, ungrouped achondrites. It is also the oldest meteorite with evidence of extrusive, silica-rich volcanism, with an Al-Mg crystallization age of 4564.8 ± 0.3 Ma. It contains the highest modal abundance of free silica, with 30% tridymite by volume, and is andesitic in composition, with 61.37 wt% silica and 0.93 wt% total alkalis. The mineralogy consists of 56% plagioclase feldspar, 30% tridymite, and 14% pyroxene (clinopyroxene and orthopyroxene). The oxygen isotopic composition matches that of the Ureilites (Srinivasan et al. 2018).

Alma-A is also thought to have originated from the ureilite parent body (UPB) on the basis of similar oxygen isotopic compositions and similar feldspar compositions to those of clasts thought to be remnants of melts from the UPB. Alma-A is similar in silica content to NWA 11119, with 60.07% silica, but contains significantly more total alkalis than NWA 11119, with 7 wt% $Na_2O + K_2O$. Alma-A has a trachyandesitic composition. The mineralogy consists of 70 vol% feldspars (zoned plagioclase and anorthoclase), 20 vol% Ca-pyroxene, and 5 vol% low-Ca pyroxene. The Al-Mg age indicates the presence of Si-rich volcanism on the UPB 6.5 Ma after the formation of Ca-Al-rich inclusions (Bischoff et al., 2014).

The third silica-rich ungrouped achondrite is Graves Nunataks 06128 and 06129 (GRA 06128/9), which are paired ungrouped achondrites. The bulk composition is trachyandesitic to andesitic, with 52.2 to 57.8 wt% SiO_2 and an average of 5.74 wt% total alkalis between the different analyses. The mineralogy includes sodium-rich plagioclase (oligoclase, >75%), olivine, and two pyroxenes. The oxygen isotopic composition matches that of the brachinites, which are olivine-rich primitive achondrites. It has been age-dated to 4.526 ± 0.06 Ga, and is thought to have been formed through partial melting of a chondritic composition with Na-rich feldspar and FeO-rich silicates. (Day et al., 2009).

NWA 11575, in comparison, is closest in bulk composition to the more silica-rich compositions presented for GRA 06128/9. NWA 11119 has significantly less alkalis than NWA 11575, and Alma-A is slightly more silica and alkali rich than NWA 11575. GRA 06128/9, Alma-A, and NWA 11575 have crystallization ages between 4.56 and 4.52 Ga, although the age of NWA 11575 has not been determined. GRA 06128/9, Alma-A, and

NWA 11575 all contain chlorapatites, as well. While there are numerous similarities, there are also numerous differences between these meteorites, suggesting different origins for each of the meteorites. NWA 11575 is the only silica-rich ungrouped achondrite containing quartz and potassium feldspar. It also has pyroxene compositional trends matching that of lunar samples and martian meteorites. The oxygen isotopic values of NWA 11575 are similar to those of the LL chondrites, while Alma-A's and NWA 11119's match those of the Ureilites, and GRA 06128/9's match those of the Brachinites. This is strong evidence for igneous processes occurring on multiple bodies within the solar system from 4.568 to 4.526 Ga.

2.0 Results

2.1 Physical Characteristics of NWA 11575

The main mass of NWA 11575, Figure 1, weighs 598 grams. The exterior of the sample (left and right) has a shiny, black fusion crust covering 80% of the surface. The interior, as seen on the broken surface (middle) and the saw-cut surface (upper right), is light in color with an aphanitic texture. On the saw-cut surface, a shock melt vein is visible, oriented diagonally from the upper left to the lower right corner. A crack is seen perpendicular to the shock melt vein, oriented top to bottom. The saw-cut also revealed two large dark-colored clasts, along with multiple smaller dark-colored clasts. The light lithology makes up greater than 95% of the material and surrounds the dark clasts. The dark clasts are also shown in Figure 2, the deposit sample at the University of New Mexico, from a more direct angle. Portions of the largest dark clast from within the

deposit sample were used in this study. Thin sections containing the light lithology and the shock melt vein were also obtained from the deposit sample.

Figure 1. Main mass of NWA 11575 (©2018 Darryl Pitt / MMGM). The shiny, black fusion crust covers 80% of the surface of the main mass and is seen on the left and right, with a broken surface in the middle. A cut surface is in the upper right, which reveals two large dark-colored, angular clasts, and multiple smaller dark-colored clasts. The broken surface and the cut surface reveal the light-colored interior of NWA 11575.

Figure 2. Cut surface of the deposit sample of NWA 11575 held at UNM. Two dark-colored clasts are apparent, with numerous smaller dark-colored clasts. A shock melt vein, approximately 1 mm wide, is visible as the dark linear feature oriented from the top corner of the cut surface to just below the dark clast.

The contact between the dark clast and the light lithology appears sharp in hand sample. Backscatter electron (BSE) images, such as Figure 3, reveal that while the contact is sharp, the contact is not as linear as it appears in hand sample. In figure 3, a large pyroxene crystal within the dark lithology is cross-cut by the light lithology, labeled a. Figure 3 also reveals what appear to be clasts or pockets of dark lithology within the light lithology along the contact. The opposite, in which there is a pocket of light lithology within the dark lithology, is also visible in Figure 4. These pockets of material are just surface irregularities, perhaps vesicles, where the meteorite is cut at an angle that distorts the relationship between the two materials directly along the contact. There are clasts of dark lithology material further from the contact, however, which are likely to be true clasts.

The morphological distinctions between the dark lithology pyroxenes and those of the light lithology are also evident in figure 3; the dark lithology pyroxenes are much more euhedral than the light lithology pyroxenes. The dark lithology also contains hopper pyroxenes, which are large euhedral crystals that formed very rapidly, and thus, failed to crystalize in the interior of the crystal. Compositional variations in the pyroxenes of the dark lithology occur amongst the larger pyroxenes and the smaller pyroxenes. Compositional zoning within the pyroxene crystals occurs near the edges and along cracks within the pyroxene crystals. Within the host lithology, the pyroxenes are much more distinctly zoned, with high contrast in BSE images, and the zoning occurs over a greater width within the crystal. The smaller pyroxene crystals within the host lithology tend to be ferropigeonite, while the larger crystals display the full range of chemical compositions present in NWA 11575's pyroxenes.

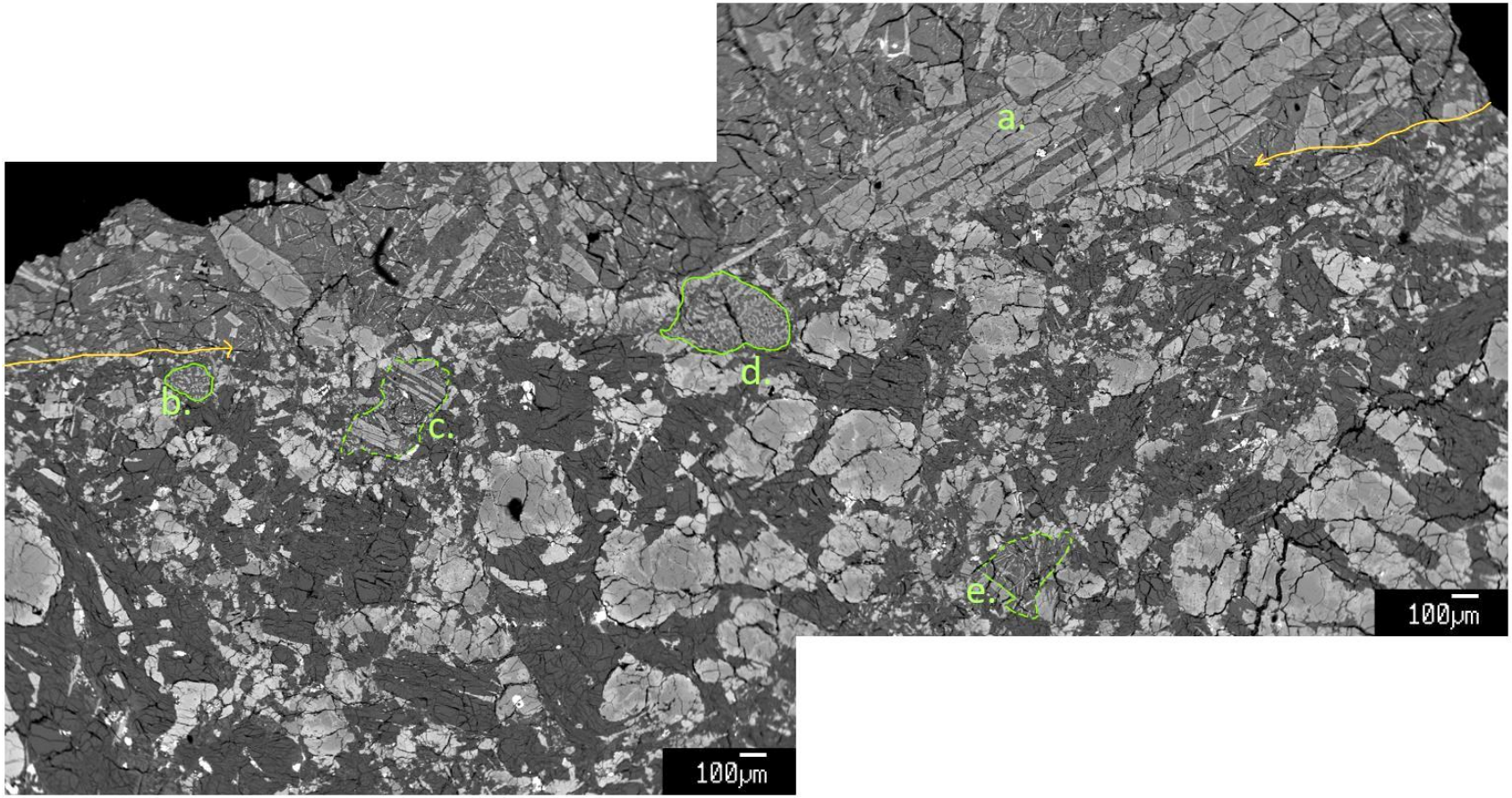

Figure 3. BSE image of the contact between the host lithology and the dark lithology. The dark lithology appears lighter in color and contains hopper pyroxenes. It is located in the upper third of the image. The light lithology contains more distinctly zoned pyroxenes surrounded by plagioclase and is in the lower two-thirds of the image. The contact is partially marked with yellow arrows. A pyroxene that has been cross-cut by the light lithology is labeled a. Labels b through e indicate areas of dark lithology within the host lithology. Dotted lines were used when the boundaries are indistinct.

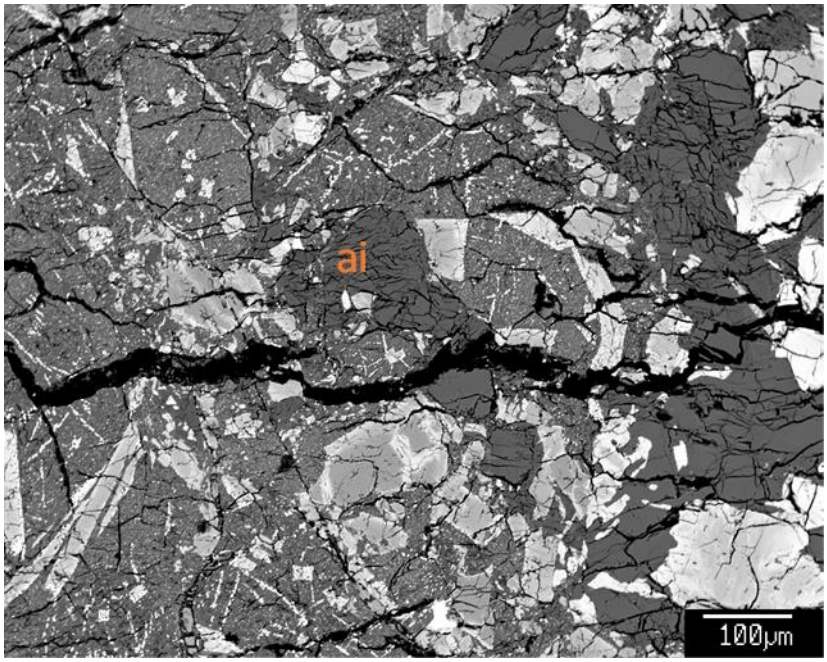

Figure 4. BSE image showing apparent inclusions. The apparent inclusion is actually the result of surface irregularities along the contact that appear as clasts of material within the other lithology, due to the angle at which the meteorite has been cut. The dark lithology is present on the left, with the light lithology on the right. In the center of the image, labeled ai, an apparent inclusion of feldspar from the light lithology is present within the dark lithology.

2.2 Mineralogy and Petrology of the Host Lithology

The mineralogy of the host lithology consists of 53.8% oligoclase (by volume), 34.1% pyroxene, 4.8% potassium feldspar, 3.8% quartz, and 2.6% apatite and merrillite, along with minor chromite, ilmenite, iron oxide, iron sulfide, and low-Ni iron. Mineral abundances were determined using element maps and the thresholding tools in Fiji. Figure 5 displays two of the RGB element maps that were used to determine the modal abundances. Figure 5 also illustrates the ophitic texture present in the host lithology, which is defined by the pyroxene crystals being less numerous than the feldspar crystals, but with the pyroxene crystals typically being larger than the feldspar crystals. The pyroxene crystals tend to be 200-500 µm in size, but larger elongate crystals have been found up to 2 mm in length. NWA11575 is a single-pyroxene rock, but the pyroxenes

show igneous zoning through magnesian pigeonite, augite, and ferropigeonite compositions. Figure 6 contains two RGB element maps of a region within the host lithology that contains euhedral to subhedral, elongate pyroxene crystals, surrounded by smaller subhedral to anhedral feldspar crystals, providing another example of the ophitic texture present within the host lithology of NWA 11575.

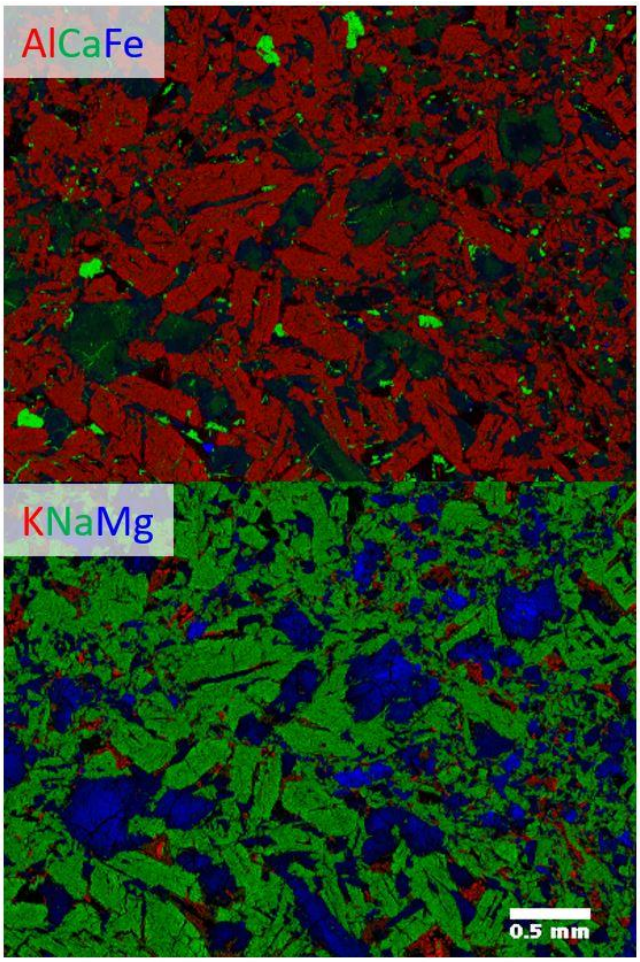

Figure 5. RGB element maps of a representative region of NWA 11575. The upper portion of the figure shows Al in red, Ca in green, and Fe in blue. Plagioclase feldspars are displayed in red, apatite and calcite veins in bright green, pyroxene in the fainter green color, and iron, iron oxides, or iron sulfides are shown in blue. The lower portion of the figure shows K in red, Na in green, and Mg in blue. Potassium feldspar feldspars appear in red, the plagioclase feldspars appear in green, and the pyroxenes appear in blue.

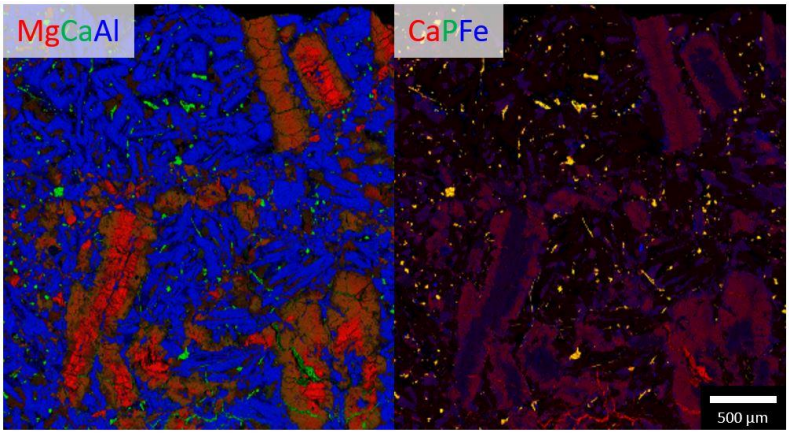

Figure 6. RGB element maps displaying an ophitic texture within the host lithology. On the left, Mg is displayed in red, Ca in green, and Al in blue. The magnesian pigeonite cores of the pyroxenes are displayed in red and the augite composition appears faintly green. Apatite and calcite veins are displayed in green, and the plagioclase feldspars are displayed in blue. In the figure to the right, Ca is displayed in red, P in green, and Fe in blue, resulting in the apatite being displayed in yellow, distinguishing the apatite from the calcite veins, which appear as a bright red.

Compositional zoning within the pyroxene crystals occurs as magnesian pigeonite cores, mantled by augite, and finally rimmed by ferropigeonite. The cores are magnesian pigeonite, $Fs_{28.4\pm4.4}$ $Wo_{8.7\pm3.7}$, Fe/Mn 36±3, n=38. The intermediate composition is augite $Fs_{30.1\pm11.6}$ $Wo_{28.3\pm4.4}$, Fe/Mn=37±6, n=90, and the rims are ferropigeonite $Fs_{58.1\pm4.6}$ $Wo_{14.3\pm2.3}$, Fe/Mn=48±3, n=98. For representative analyses, averages, and standard deviations of the pyroxene analyses, see Table 1 in the Appendix. Figure 7 displays the pyroxene quadrilateral for the host lithology.

The pyroxene quadrilateral displays three distinct compositions of pyroxenes, with few intermediate analyses, suggesting that the crystallization of pyroxene occurred rapidly to record the changing chemical composition of the magma. The zoning appears abrupt, also supporting the interpretation of rapid crystallization and rapid magma composition change. Igneous zonation can typically be expected to occur as layers throughout the entire crystal, reminiscent of tree rings. In NWA 11575, however, the

zonation is often truncated, as shown in Figure 8. Figure 8b shows one pyroxene crystal with the typical zonation on one end, and truncated zonation on the other end of the crystal. The truncated zonation is not consistent with chemical disequilibrium and is instead likely the result of a mechanical disturbance. The zonation within the crystal also suggests the degree and style of crystallization. The magnesian pigeonite core is euhedral, while the ferropigeonite rim extends out into what must have been open spaces along the mineral's boundary, transitioning to a more anhedral grain boundary as the crystal continued to grow. This transition and the truncation of the pyroxene zonation suggests that an eruption occurred, which caused a mechanical disruption of the pyroxene crystals prior to crystallization of the ferroan pigeonite rims. This explains the anhedral nature of the ferropigeonite rims and the occurrence of many small ferropigeonite crystals.

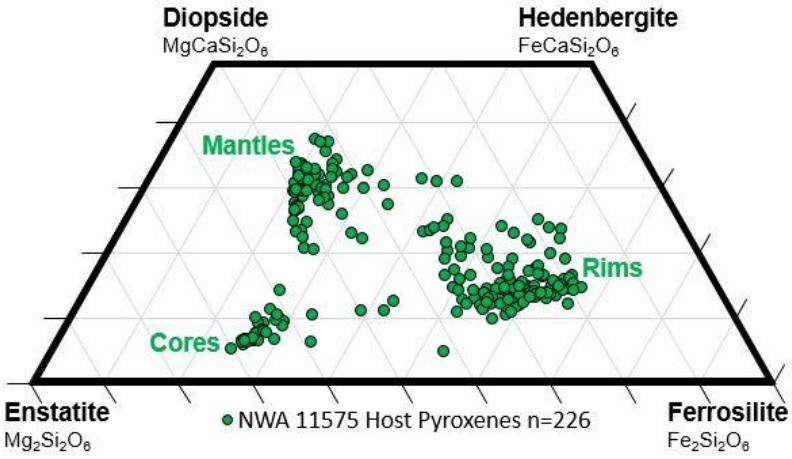

Figure 7. Pyroxene quadrilateral of host lithology pyroxenes. The zonation begins with magnesian pigeonite cores, rapidly progresses to augite, and then the rim composition is ferropigeonite.

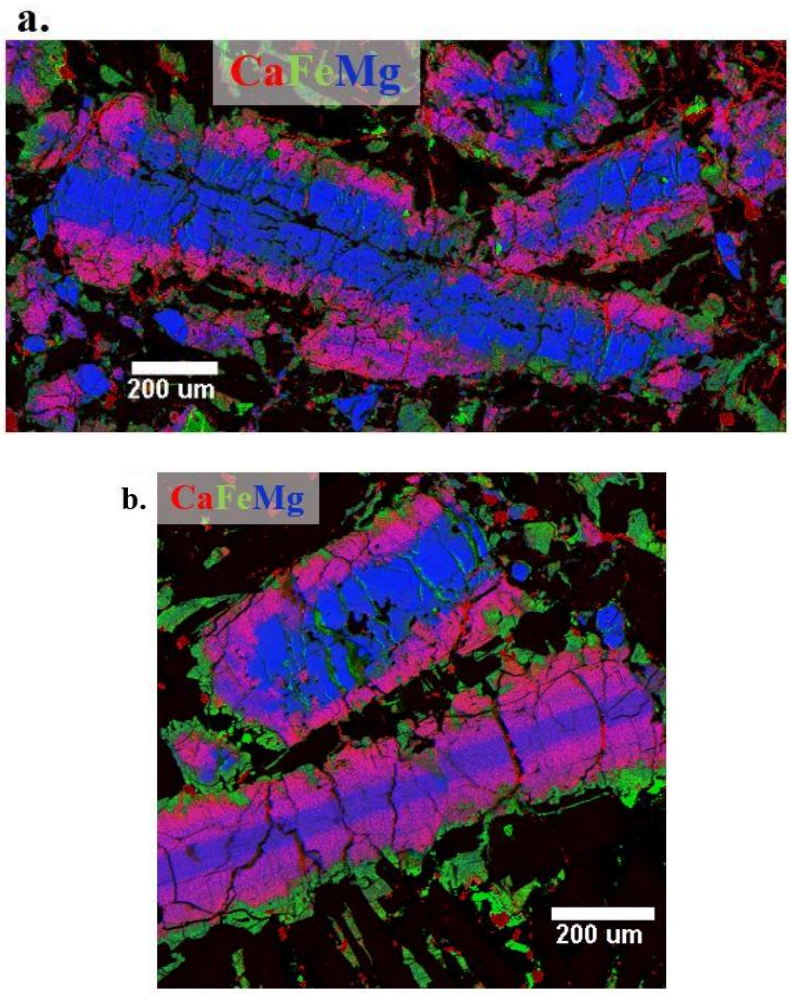

Figure 8. RGB element maps of pyroxene crystals in the host lithology of NWA 11575. Ca is in red, Fe is in green, and Mg is in blue in both 8a and 8b. The large pyroxene crystal in fig. a and both crystals in fig. b show the truncated zonation. The upper crystal in fig. b is only truncated on the right side. The left side shows a normal, igneous zonation.

In addition to the igneous zonation, exsolution and chemical zoning is present in the host lithology pyroxenes. Exsolution is present, although very rare, within the pyroxene crystals, as seen in Figure 9a. Zoning along cracks, possibly a result of alteration by a fluid, is common along the edges and cracks within pyroxene crystals, as shown in Figure 9b.

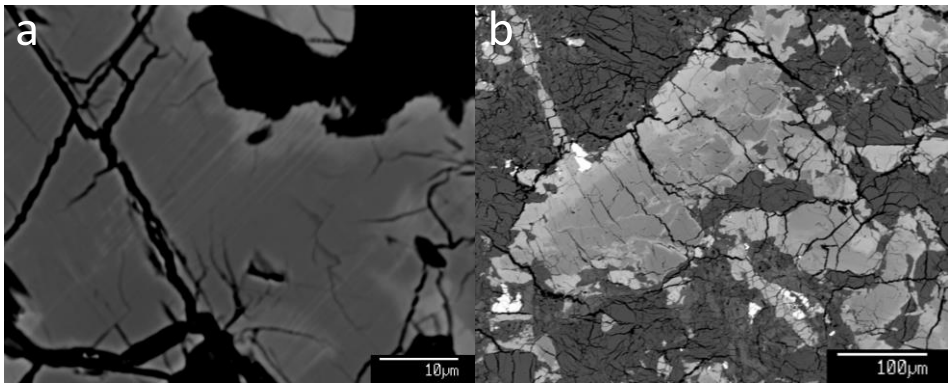

Figure 9. BSE images showing exsolution and zoning along cracks in pyroxenes. a) BSE image showing exsolution with a pyroxene in the host lithology. b) BSE image showing evidence of compositional zoning along cracks within the pyroxene crystal, which suggests alteration by a fluid after crystallization.

The oligoclase composition is fairly consistent throughout the sample, with $Ab_{81.5\pm2.2}$ $An_{17.2\pm2.3}$ $Or_{1.4\pm0.2}$, n=44. The potassium feldspar composition is fairly constant with 44 out of 49 analyses having between 12.03 wt% K_2O and 16.62 wt% K_2O, corresponding to $Ab_{3.8\pm0.9}$ $An_{0.4\pm0.3}$ $Or_{95.8\pm1.1}$, n=44. The remaining five analyses range in K_2O from 4.30 to 14.31 wt%. The composition for all of the potassium feldspar is $Ab_{7.8\pm12.1}$ $An_{0.5\pm0.3}$ $Or_{91.8\pm12.2}$, n=49, which poorly represents the majority of potassium feldspar in NWA 11575, due to the extreme range in composition for the other five potassium feldspar analyses. Figure 10 displays the feldspar ternary for feldspars within the host lithology and Table 2 in the Appendix presents the average, standard deviation, and representative electron microprobe analyses of feldspars within the host lithology. The oligoclase feldspar crystals do not exhibit compositional zoning and are subhedral to anhedral. The potassium feldspar occurs mostly as an exsolved phase from the oligoclase feldspar, and occurs only rarely with a distinct crystal habit, but is still associated with the oligoclase feldspar, as shown in figure 11.

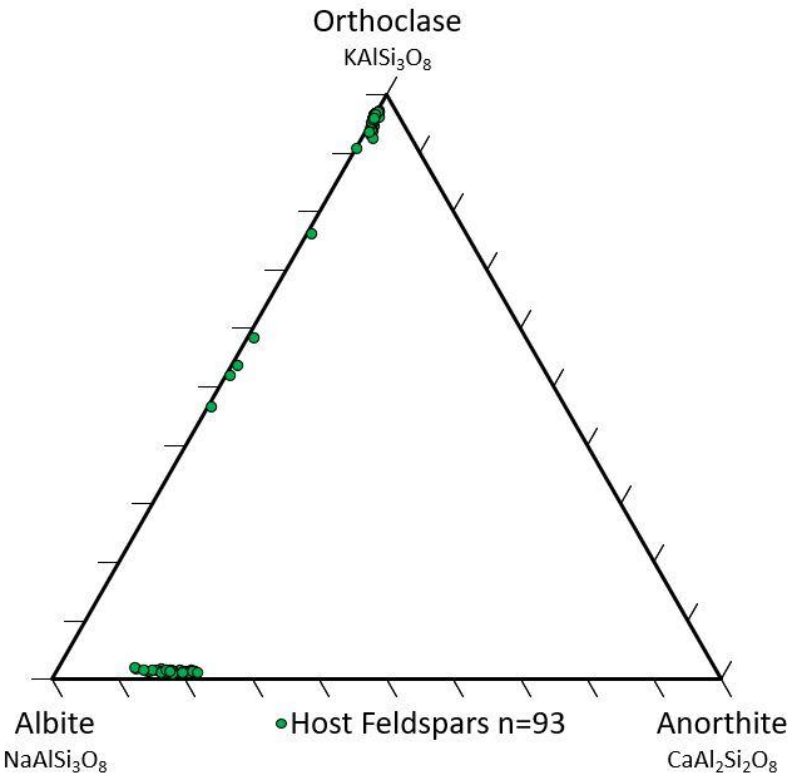

Figure 10. Feldspar ternary displaying the compositions of the potassium feldspar and oligoclase within the host lithology.

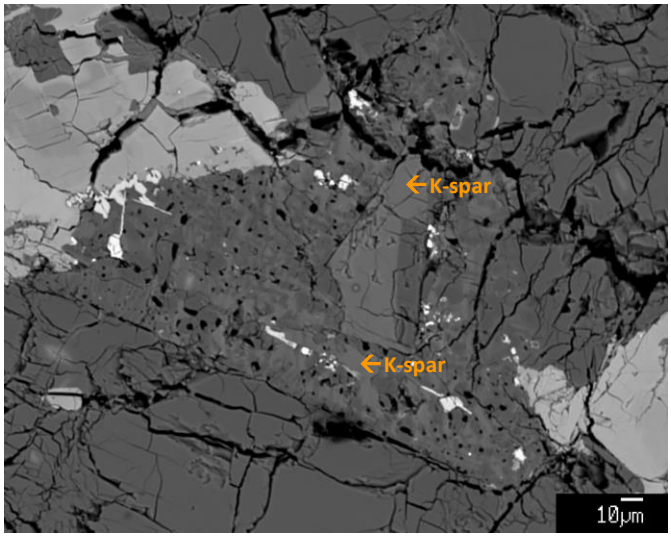

Figure 11. BSE image of oligoclase with potassium feldspar exsolution. The oligoclase appears as the dark grey phase, while the potassium feldspar is the medium grey phase, labeled K-spar. Also apparent are numerous vesicles present within the potassium feldspar and oligoclase. Quartz is not present.

The potassium feldspar and quartz are also found in contact with each other, such as in figure 12, in which quartz is surrounded by potassium feldspar. The potassium feldspar and quartz also occur as a fine intergrowth, as illustrated in figure 13, with a micrographic texture. In the regions with the micrographic texture, apatite, low-Ni iron metal, iron-oxide, troilite, chromite, and ilmenite are also commonly found. These regions are interpreted to be disequilibrium assemblages representing the residual melt, or mesostasis, as a result of either eutectic crystallization or significant undercooling. The quartz is always found to be in contact with the potassium feldspar, although the potassium feldspar can be found without the quartz. The presence of quartz has been determined by X-ray diffraction (XRD). Due to the overlap of cristobalite and pigeonite peaks, the presence of cristobalite in addition to the quartz is uncertain.

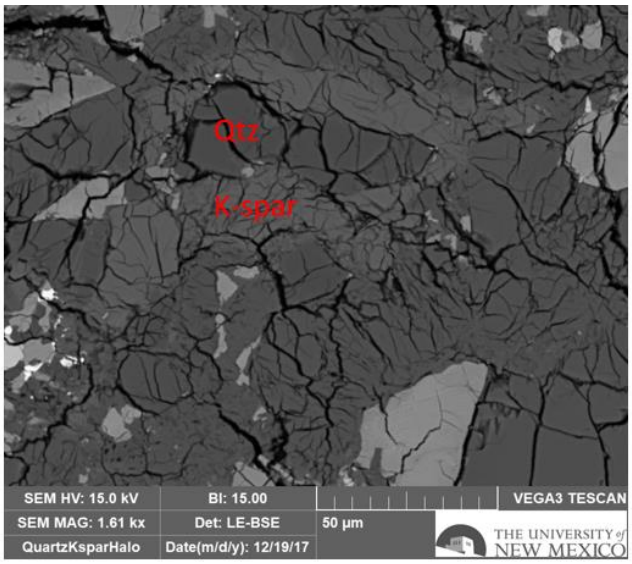

Figure 12. BSE image of quartz surrounded by potassium feldspar. The quartz and oligoclase appear the same dark grey color in BSE images.

Apatite and merrillite within the host lithology account for 2.6% of the meteorite by volume. All of the apatite in the host lithology is chlorapatite, with 81% of the X-site

filled with Cl, equating to 5.55 ± 0.27 wt% and F content varies from below detection limits to 0.19 wt% F. The F in the X-site only accounts for an additional 1%, with 18% thus being a missing component. OH accounts for only 5-6% of the missing component, with the remaining missing component likely comprised of O and a vacancy substitution, as observed in synthetic and natural Cl-rich apatites (Hovis and Harlov, 2010; Schettler et al., 2011; McCubbin and Ustunisik, 2018; Jones et al. 2014; Jones et al. 2016). The apatite does not display compositional zoning and is interpreted to be a primary mineral, suggested by the large size (200 microns) of some of the apatite grains and the euhedral

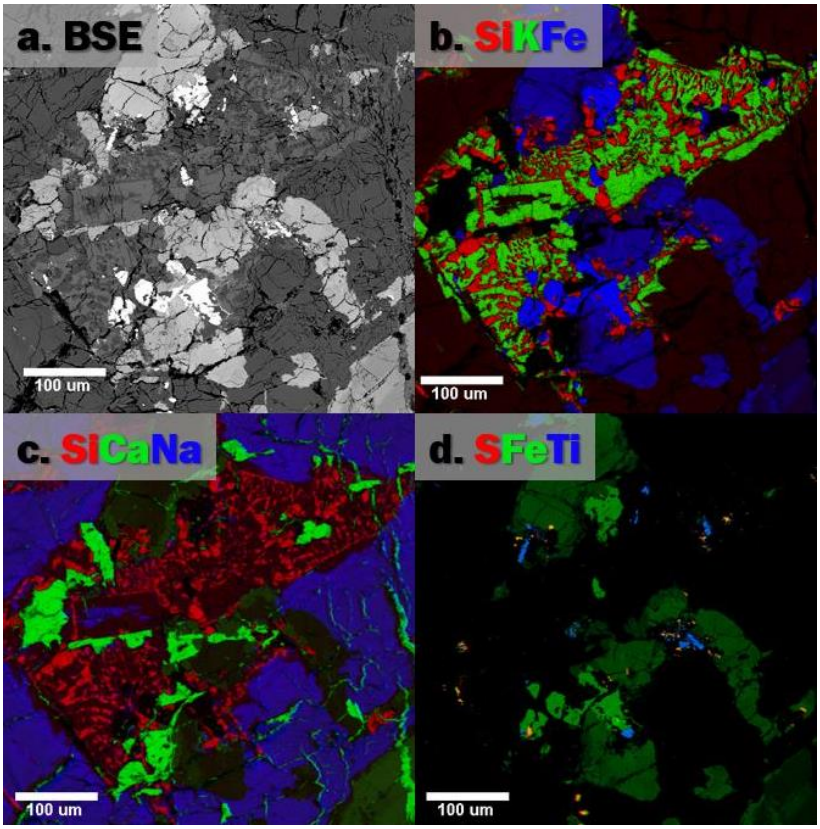

Figure 13. Backscatter Electron image and RGB element maps of mesostasis. a) BSE image of the quartz and potassium feldspar intergrowth. b) Potassium feldspar and quartz intergrowth is displayed with Si in red and K in green. c) Apatite and calcite veins are displayed in green. Na is displayed in blue, showing the Na-feldspar core in the euhedral potassium feldspar crystal near the center. d) Ilmenite is shown in light blue, and troilite is shown in orange.

crystal habit sometimes observed. The crystal habit of the apatite ranges from euhedral and anhedral. Apatite is more abundant than merrillite by a factor of three. The merrillite and apatite occur as individual grains, except in at least one case where the merrillite and apatite are found within the same crystal. Table 3 in the appendix contains representative electron microprobe analyses of apatite from within the host lithology, as well as the average and standard deviation. Figure 14 is a ternary diagram showing the Cl-F-OH composition of the apatite within the host lithology, as well as the compositions of apatites from H, L, and LL ordinary chondrites, and GRA 06128/9. The apatite is similar in composition to the ordinary chondrites and GRA 06128/9 but contains less fluorine. The apatite appears often in association with the disequilibrium assemblages but appears to be ubiquitous throughout the light lithology. The apatite ranges in size from a micron to over 200 microns and is often acicular. Figure 15 suggests that the apatite crystallized after the plagioclase. The apatite sizes form distinct groups, with a small percentage of apatite crystals on the order of 100 microns, and the majority being small apatites, on the order of a few microns. The smaller apatites seem to occur within the disequilibrium assemblages, suggesting that they may have formed later than the larger apatites. Further study is needed to ascertain whether or not there are two populations of apatites that crystallized at different times. Figure 15 shows one of the larger apatites that is not surrounded by the potassium feldspar silica intergrowth. Instead, it is next to a euhedral feldspar and is in contact with several ferropigeonites. Figure 16 shows a BSE and RGB element map of an apatite crystal that is surrounded by the potassium feldspar and quartz intergrowth. Also present is an iron phase and ilmenite, located within the potassium feldspar and quartz intergrowth.

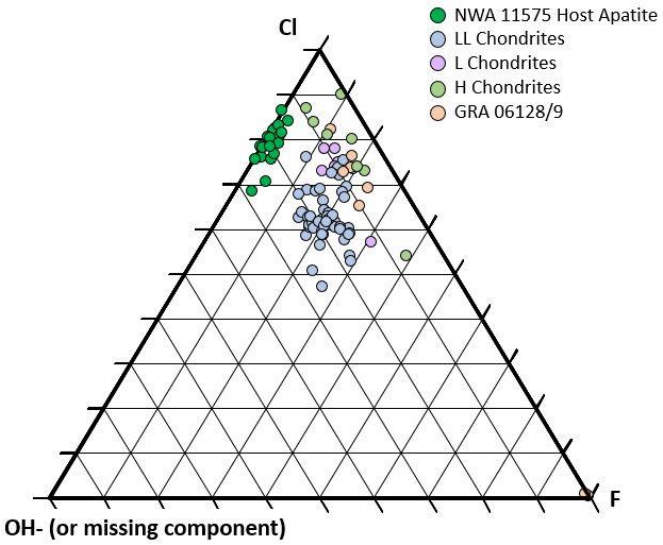

Figure 14. Cl-F-OH- ternary diagram of NWA 11575 host lithology apatites and apatites from ordinary chondrites and GRA 06128/9. The OH^- component is calculated by $OH^-=(1-Cl-F)$ with Cl and F being measured in formula units. Data for the H chondrites is from Jones et al. (2016). Data for the L chondrites is from Lewis & Jones (2016). Data from the LL chondrites is from Jones et al. (2014), and data from GRA06128/9 is from Shearer et al. (2011).

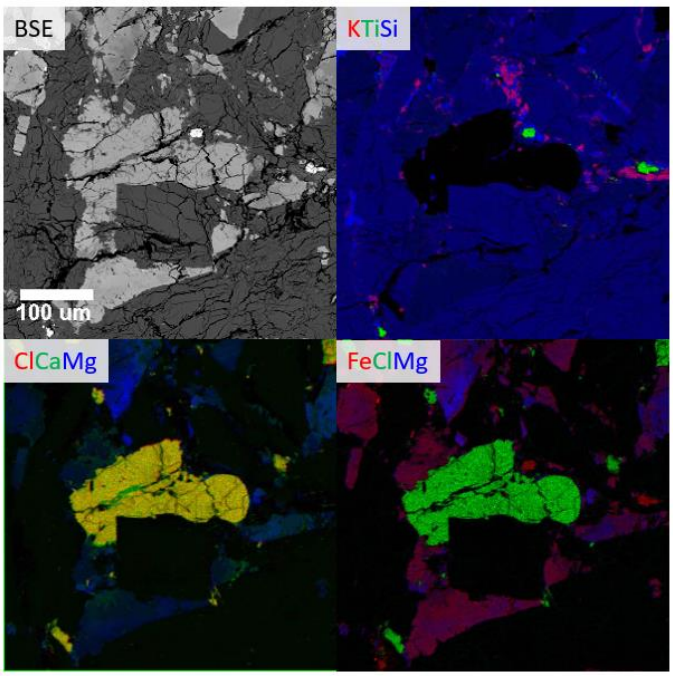

Figure 15. BSE image and RGB element maps of a large apatite within the host lithology. The apatite is approximately 200 microns x 100 microns. The feldspar is the dark grey phase in BSE, and the apatite is best identifiable in the RGB maps showing Cl or Ca. Potassium feldspar is present in the upper right RGB map and is displayed in red.

Two apatite crystals and one merrillite crystal were analyzed for H_2O content and δD using nanoSIMS. The apatite crystals contained 944 and 1098 ppm H_2O, and the δD measured +87±110‰ and -173±218‰. The merrillite contained 1773 ppm and the δD value measured +23±76‰. Figure 17 shows δD ‰ values for apatite and merrillite from NWA 11575, along with the values from Jupiter, martian meteorites, bulk Earth, carbonaceous chondrites, and ordinary chondrites. The δD values overlap with ordinary and carbonaceous chondrites, Vesta, and samples from Earth. It has been suggested that the Earth's source of water could have been hydrous CM chondrites (Sharp, 2018), which could be the case for NWA 11575, because the δD of NWA 11575 apatite and merrillite are similar to the bulk Earth values. This is assuming that NWA 11575 formed within the snow-line. If we assume that NWA 11575 formed outside of the snow line, it would simply represent the composition of the water in the region where NWA 11575 formed.

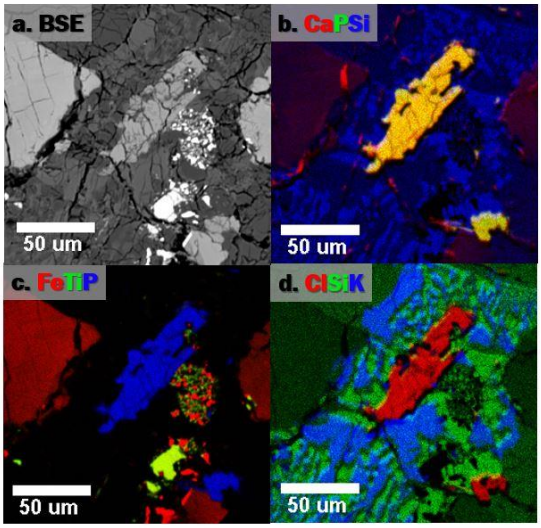

Figure 16. Apatite located within a region of silica and potassium feldspar intergrowths. a) BSE image. b) RGB element map with Ca in red, P in green, and Si in blue. The apatite appears in yellow and the quartz in blue. c) RGB element map showing Fe in red, Ti in green, and P in blue. The apatite appears in blue, pyroxene and iron phases in red, and ilmenite appears in a yellow-green color. d) RGB element map with Cl in red, Si in green, and K in blue. This shows the intergrowth of the potassium feldspar and quartz.

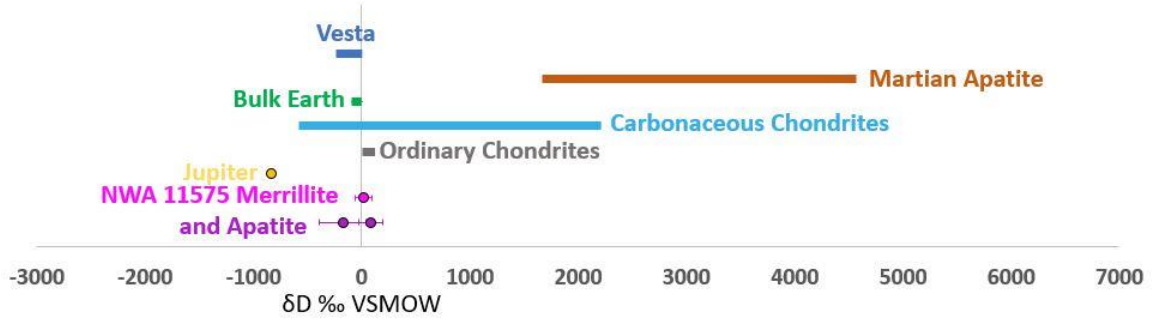

Figure 17. Comparison of δD‰ of NWA 11575 apatite and merrillite with other planetary bodies. The range of hydrogen isotopic compositions are shown for apatites from martian meteorites, carbonaceous chondrites, ordinary chondrites, Vesta, and Earth. The data for Jupiter and the data from NWA 11575 are represented by the value and the 1σ and 2σ error, respectively. Data from Sharp (2017), Robert et al. (2000), Mahaffy et al., (1998), and Hallis (2016).

2.3 Mineralogy and Petrology of the Dark Clast

The dark lithology consists of 70% groundmass and 30% pyroxene, with trace amounts of low Ni iron and iron oxides (less than 1% combined). Apatite is also present within the dark lithology but is not ubiquitous, and thus the abundance has not been determined. Tables 4, 5, and 6 in the appendix contain representative analyses, averages, and standard deviations for analyses of the groundmass, pyroxenes, and apatites from the dark lithology.

The pyroxenes occur as two different morphologies: 1) large pyroxenes approximately 200 microns or greater in diameter, with a hopper morphology or 2) smaller, euhedral pyroxene crystals, approximately 50 microns in diameter. Both morphologies of pyroxene crystals appear to be zoned near the edges of the crystal, as is evident in Figure 18.

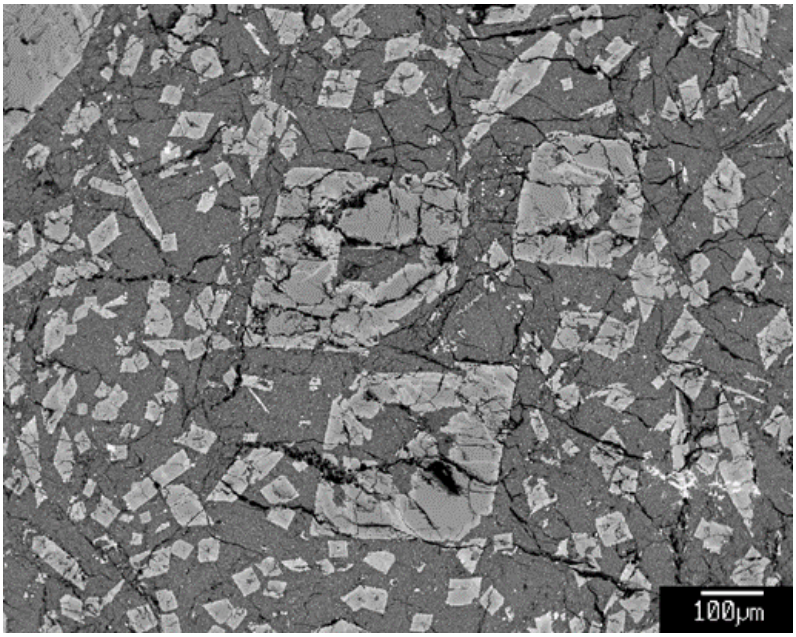

Figure 18. Backscatter electron image of the pyroxenes within the dark lithology of NWA 11575. The three larger pyroxenes in the center of the image are hopper pyroxenes, where the interior of the crystals contains groundmass, because the crystal formed very rapidly and the interior did not fully crystallize. The other pyroxenes are significantly smaller. Both large and small pyroxenes show compositional zoning just near the edge of the crystals.

The compositional trend of the pyroxenes in the dark lithology is very similar to that of the light lithology (see Figure 19). However, the compositional trend did not advance to the ferropigeonite composition, and the change in composition occurs between the large and small pyroxenes. The large hopper pyroxenes are magnesian pigeonite, while the smaller pyroxenes are augitic. A transect across one of the large hopper pyroxenes revealed no compositional zoning, with an average composition of $Wo_{(5.8\pm0.3)}$, $Fs_{(26.2\pm0.9)}$, with seven analyses across the pyroxene crystal. The pyroxene compositions within the dark lithology are magnesian pigeonite $Wo_{(8.1\pm4.5)}$, $Fs_{(27.1\pm2.8)}$, Fe/Mn 37±2, n= 34, and augite $Wo_{(31.0\pm3.7)}$, $Fs_{(29.1\pm7.6)}$, Fe/Mn 37±4, n=53.

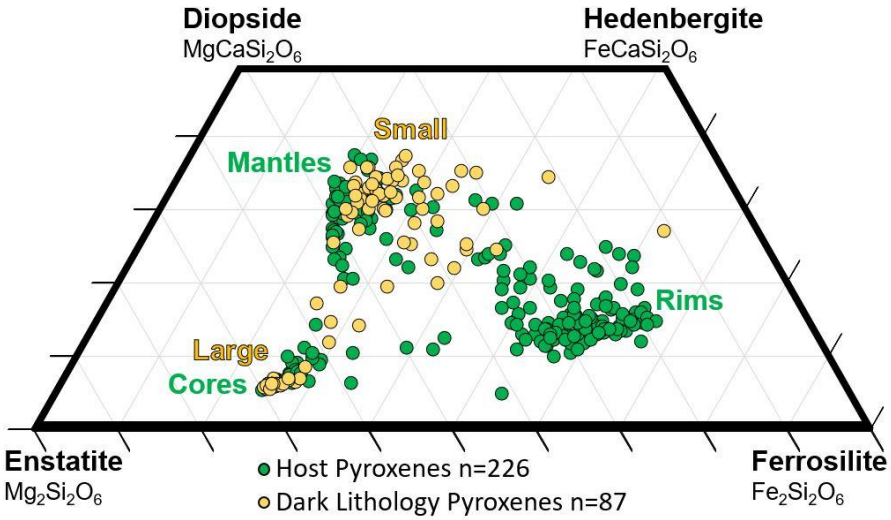

Figure 19. Pyroxene quadrilateral comparing the dark and host lithologies' pyroxenes compositions. The dark lithology pyroxenes show a compositional trend between the large hopper pyroxenes and the small pyroxenes, with the large pyroxene compositions matching that of the host lithology pyroxenes' cores (magnesian pigeonite). The small pyroxenes within the dark lithology are augite.

The groundmass is similar in composition to feldspar, with high SiO_2 (62.06 wt%), Al_2O_3 (15.12 wt%), and Na_2O (8.67 wt%), but also contains an average of 7.28 wt% FeO. The average and standard deviation of analyses of the groundmass can be found in Table 4 in the Appendix. The groundmass is interpreted to be a quenched glass, as is supported by the quench texture seen in figure 20, showing unequilibrated olivine within the groundmass. The apatite within the dark lithology is also chlorapatite. It was found within the dark lithology near the contact between the host and dark lithologies, but was not found in a larger thin section of the dark lithology. Because the apatite is not ubiquitous within the dark lithology, more work is required to determine the abundance of this phase and the connection between the apatite within the host and dark lithologies. Apatite is typically one of the last phases to crystalize, so its presence within the dark lithology is unexpected, since the dark lithology contains only euhedral pyroxenes and

the quenched groundmass. Figure 21 is a BSE image of chlorapatite within the dark lithology.

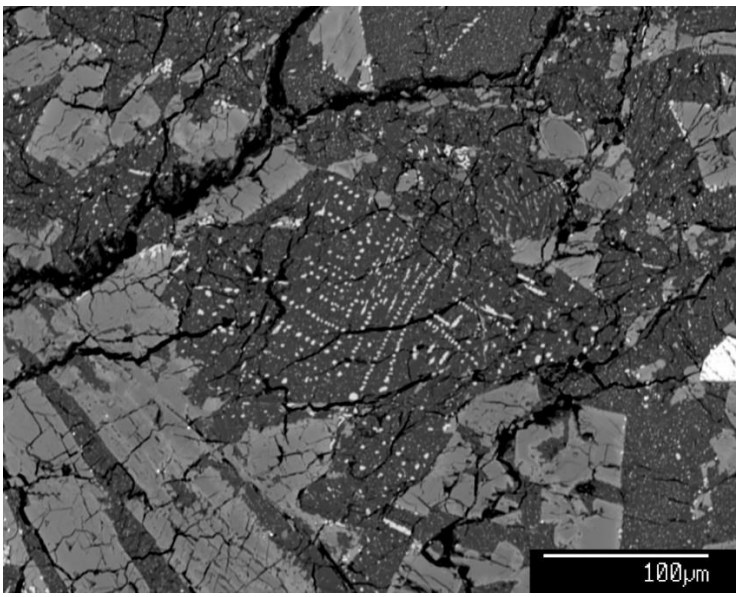

Figure 20. BSE image of the groundmass within the dark lithology. The bright phase in the dark grey phase (groundmass) is the unequilibrated olivine. The medium grey phase is pyroxene.

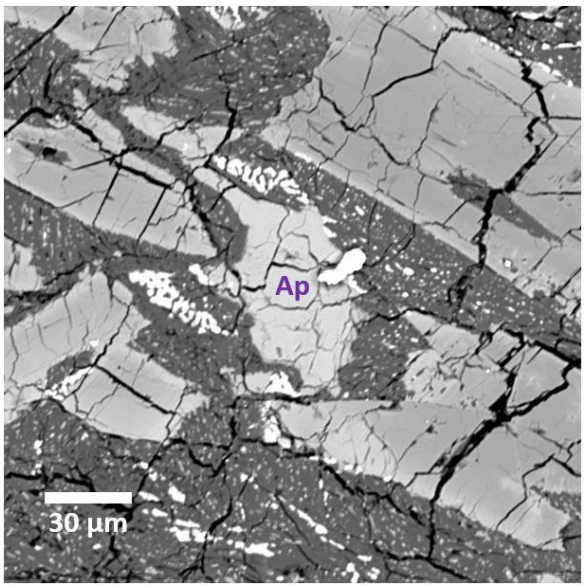

Figure 21. BSE image of an apatite crystal within the dark lithology, labeled Ap.

2.4 Fe/Mn of Pyroxenes from the Host and Dark Lithologies

Fe/Mn ratios within pyroxenes from the host lithology range from 36±3 in the magnesian pigeonite cores, to 37±6 in the augitic mantles, to 48±3 for the ferropigeonite rims. The Fe/Mn ratios of the pyroxenes within the dark lithology are on average 37±2 for the magnesian pigeonite and 37±4 for the augite. The host lithology shows a greater range in Fe/Mn ratios, as can be seen in Figure 22, a plot of Fe versus Mn (in atomic formula units). Additionally, the host and the dark lithology plot along the same line, which plots in between that of Mars, Earth, and the Moon. This suggests that the host and dark lithologies are derived from the same parent body, but the dark lithology pyroxene compositions did not evolve to the ferropigeonite composition that is responsible for the higher Fe/Mn ratios within the host lithology.

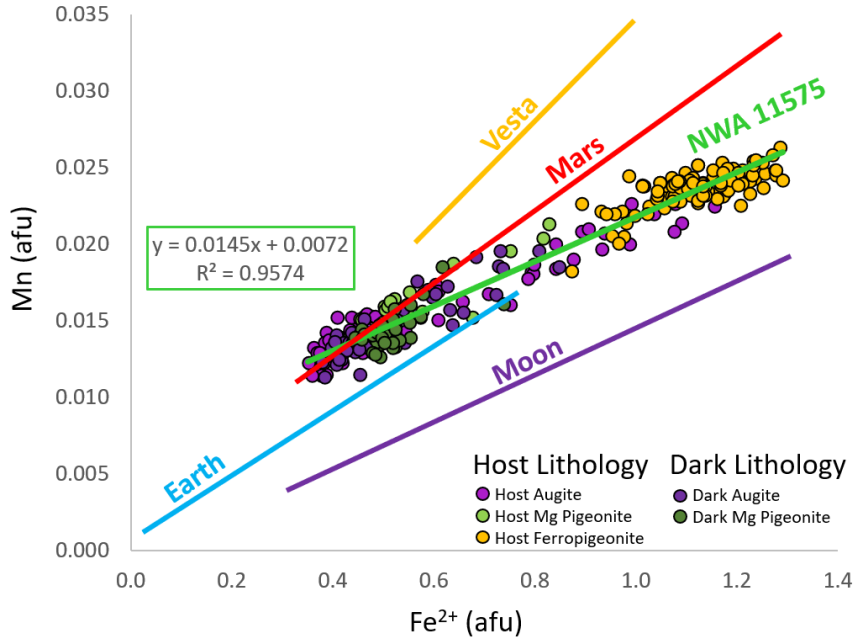

Figure 22. Fe^{2+} versus Mn of pyroxenes within the host and dark lithologies of NWA 11575, along with those of pyroxenes from Earth, Moon, Mars, and Vesta (after Papike et al., 2009). Fe and Mn are presented in atomic formula units and have been corrected for the presence of Fe^{3+}, as described by Droop (1987). The trendline presented for NWA 11575 accounts for all data points from the host and dark lithologies.

2.5 Bulk Compositions of the Host and Dark Lithologies

The shock melt vein, which runs through the host lithology, represents the bulk lithology's composition assuming that all of the phases present in the host lithology melted at the same rate and were incorporated in the melt vein in the ratios that were present within the host lithology. This assumes complete melting along the shock melt vein. Another assumption is that the shock melt vein did not incorporate any dark lithology material. The shock melt vein analyses are presented in Table 6 in the Appendix. The bulk composition of the host lithology was also determined using microprobe analyses for all major phases, along with their abundances and assumed average density. The same approach was used for determining the bulk composition of the dark lithology. The bulk composition is represented on the total-alkalis versus silica (TAS) diagram, figure 23, and in Table 7 in the appendix. The TAS diagram is utilized in igneous petrology to classify extrusive igneous rocks and can be used to describe the degree of chemical evolution of an igneous rock (Le Bas et al., 1986). The composition of the light lithology plots within the andesite field, with 58.70±0.94 wt% SiO_2, 4.82±0.20 wt% Na_2O, and 0.77±0.21 wt% K_2O. The composition of the melt vein is slightly higher in both silica and alkalis, with 60.65±1.30 wt% SiO_2, 6.27±0.47 wt% Na_2O, and 0.61±0.17 wt% K_2O, which may be a result of melting a higher proportion of feldspars relative to the pyroxenes within the shock vein. The composition of the dark lithology is within error of the light lithology melt vein, and slightly more silica- and alkali-rich than the bulk composition of the host lithology, with 60.41±1.32 wt% SiO_2, 6.36±0.49 wt% Na_2O, and 0.16±0.03 wt% K_2O.

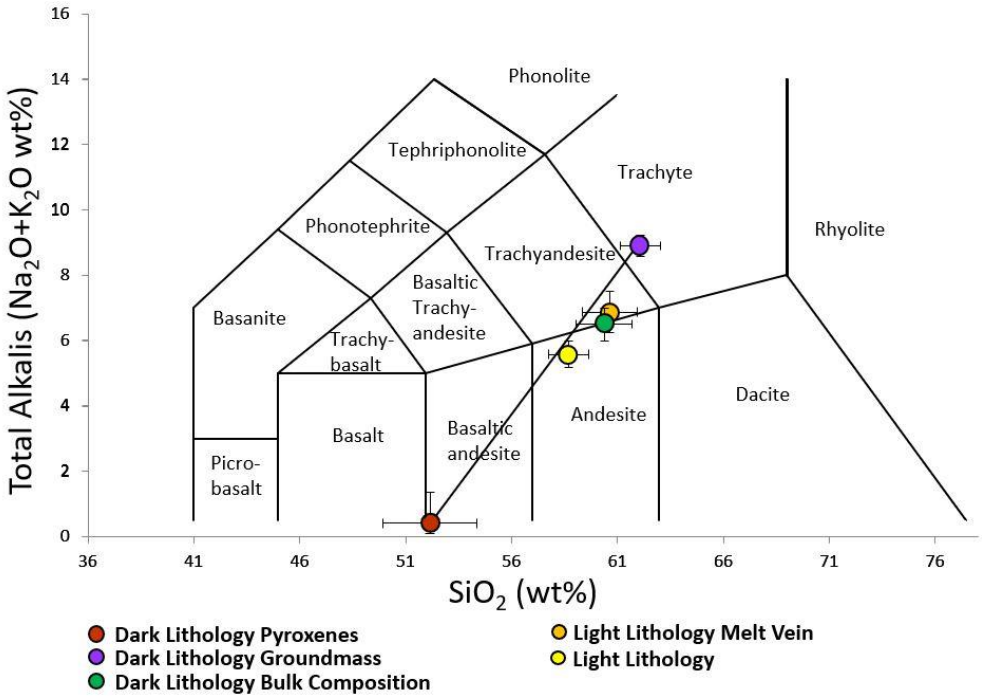

Figure 23. Total-alkalis versus silica diagram showing the bulk composition of the host and dark lithologies of NWA 11575 (after Le Bas et al., 1986). Also shown on the diagram are the average pyroxene composition and the average composition of the groundmass within the dark lithology, as well as a tie-line between the two phases. The bulk composition of the dark lithology plots within error of the tie-line. The light lithology composition is plotted in yellow, and the melt vein composition is plotted in orange.

2.6 Stable Isotope Geochemistry of the Host and Dark Lithologies

Oxygen isotopic analyses of acid-washed bulk rock samples of NWA 11575's host lithology resulted in an average $\delta^{18}O$ of 5.449±0.310‰, an average $\delta^{17}O$ of 4.063±0.165‰, and an average $\Delta^{17}O$ of 1.186±0.004‰ out of six analyses. Analyses from the non-acid-treated dark lithology material resulted in an average $\delta^{18}O$ of 5.377‰ ± 0.154, an average $\delta^{17}O$ of 4.003‰ ± 0.083, and an average $\Delta^{17}O$ of 1.164‰ ± 0.005 out of four analyses. The slopes of the linear trendlines produced by these data are 0.531 for the light lithology and 0.540 for the dark lithology, as demonstrated in Figure 24, a triple oxygen diagram. Figure 24 shows that NWA 11575 plots in the same field as LL

chondrites. The average values for LL chondrites are $\delta^{18}O = 5.026‰ \pm 0.2303$, $\delta^{17}O = 3.869‰ \pm 0.166$, and $\Delta^{17}O = 1.255‰ \pm 0.117$, with a trend line slope of 0.511 (Clayton et al., 1991). NWA 11575 occupies the same space on a triple oxygen diagram, with remarkably similar values for $\Delta^{17}O$ and the slope of the trend line, suggesting that NWA 11575 formed in the same isotopic reservoir as the LL chondrites. This also suggests that NWA 11575 may share a genetic link with LL chondrites, perhaps being derived from the LL chondrite parent body. The similar oxygen isotopic ratios between the light and dark lithologies also suggests that they share the same source material and the dark lithology is not a foreign xenolith.

Chromium isotopes are useful in identifying early-formed heterogeneities, and thus genetic links, because manganese-52 decays into chromium-53 with a half-life of 3.7 ± 0.4 my, and thus any heterogeneities in the $^{53}Cr/^{52}Cr$ must have been established in the first 20-26 my after nucleosynthesis of ^{53}Mn (Righter et al., 2006). 54-Chromium is stable. The bulk chromium stable isotope ratios for the host lithology of NWA 11575 are $\varepsilon^{53}Cr = +0.23 \pm 0.06$ and $\varepsilon^{54}Cr = -0.29 \pm 0.09$. The $\varepsilon^{54}Cr$ of NWA 11575 is similar to those of ordinary chondrites, particularly the L and LL chondrites. Warren (2011a, 2011b) noticed a bimodality between the $\varepsilon^{54}Cr$ and $\Delta^{17}O$ values of planetary materials, such as is shown in figure 25, and he proposed that this is either a result of heterogeneous accretion of materials within the protoplanetary disk or a result of isotopic differences between the inner and outer solar system during planetary formation. However, regardless of whether it does represent a divide between the inner and outer solar system, the bimodality differentiates between carbonaceous and non-carbonaceous materials (Warren, 2011b). Furthermore, the agreement of the chromium and oxygen isotopic

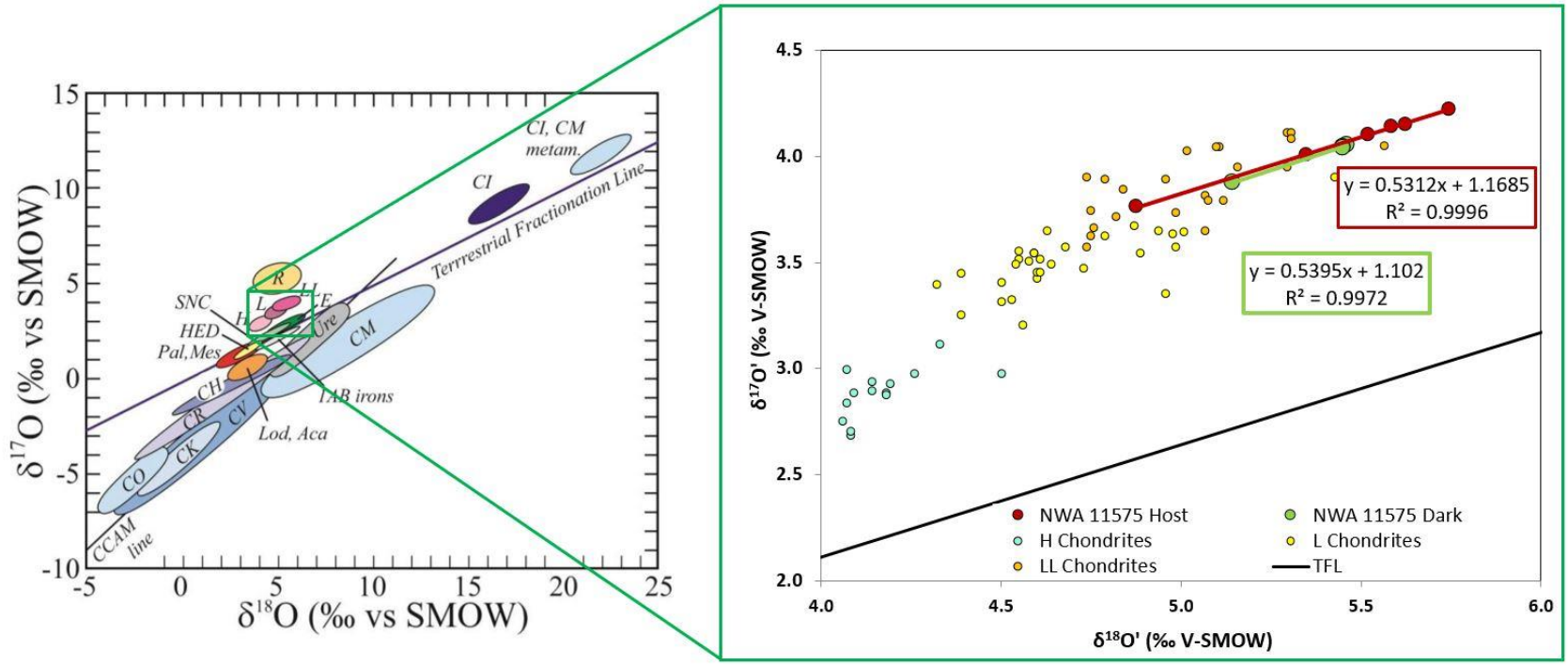

Figure 24. Triple oxygen diagrams showing the analyses from NWA 11575's host and dark lithologies. Also shown are analyses of the ordinary chondrites (Clayton et al., 1991). The left portion of the diagram shows the location of the ordinary chondrite fields relative to other analyzed meteorite groups or bodies (modified from Sharp et al., 2018). The equations for the lines of best fit for the host and dark lithologies are shown in the red and green boxes, respectively. The TFL line is the Terrestrial Fractionation Line, along which all samples from the earth and the moon plot.

systems strengthens the argument that NWA 11575 formed in the same isotopic reservoir as the LL chondrites.

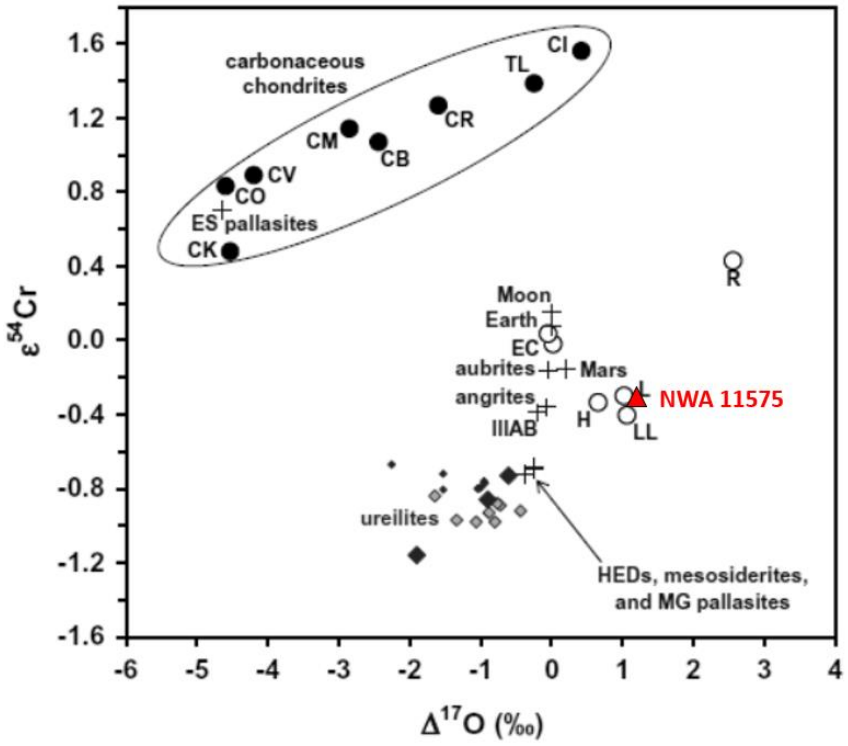

Figure 25. Δ17O versus ε54Cr of planetary materials. The bimodality in oxygen and chromium isotopic compositions can be seen between the carbonaceous chondrites and ureilites, HEDs, ordinary chondrites, the Earth, the Moon, Mars, Enstatite chondrites, aubrites, angrites, and R chondrites. The bimodality has been proposed to have resulted from formation within the inner and outer solar system, with the carbonaceous chondrites being formed in the outer solar system and the other grouping to have formed in the inner solar system. Figure modified from Warren, (2011a).

2.7 Rare Earth Elements

Rare earth element (REE) patterns were obtained for the bulk light lithology and the bulk dark lithology from raster analyses using Laser Ablative Inductively Coupled Mass Spectrometry (LA-ICP-MS). The analyses, normalized to chondritic values, can be seen in figure 26. $(La/Lu)_N$ is 1.22 for the light lithology, and the dark lithology has a $(La/Lu)_N$ of 1.17. These values indicate negative slopes for the light and dark lithologies'

REE patterns, and thus are indicative of slight LREE enrichment and HREE depletion. In comparison to the other silica-rich ungrouped achondrites, NWA 11575 has a slight negative slope, comparable to that of GRA 06128/9, while NWA 11119 and Alma-A both show positive slopes. The REE patterns for NWA 11575 show elevated concentrations from those of the ordinary chondrites, which can be expected for a liquid that has undergone significant fractional crystallization. The host and dark lithologies both have a negative europium anomaly. The host lithology has a negative europium anomaly of 0.57, and the dark lithology has a negative europium anomaly of 0.84. GRA 06128/9, Alma-A, and NWA 11119 all have positive europium anomalies, as can be expected for a rock containing significant amounts of plagioclase.

The negative europium anomaly in the whole rock data for the light and dark lithologies could suggest that there was removal of plagioclase from the bulk rock. The Eu^{2+} substitutes for Ca2+ in the plagioclase structure, due to having a similar size and charge, so plagioclase carries the positive europium anomaly. However, if significant amounts of plagioclase were removed, the bulk rock could still have a negative europium anomaly. This could explain the lack of zoning in the plagioclase crystals, as perhaps the early-formed plagioclase crystals, which likely would have been rich in Ca, were removed.

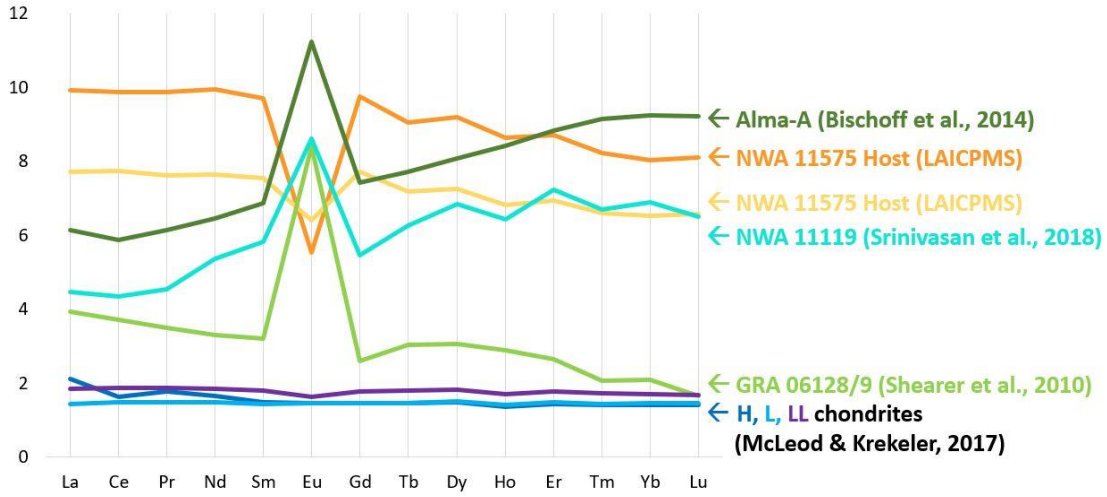

Figure 26. Rare Earth Element analyses of NWA 11575, the silica rich ungrouped achondrites, and ordinary chondrites. For the silica-rich ungrouped achondrites and the ordinary chondrites, references are listed in parentheses.

Ni and Co are both highly compatible elements and a depletion in these elements suggests a high degree of fractionation. CI chondrites contain on average 10640 ppm Ni and 502 ppm Co, to produce a Ni/Co ratio of 21.2 (Lodders, 2003). The Ni abundance in NWA 11575 is 5 ppm Ni, while the Co abundance is 13 ppm. The Ni/Co of the bulk host lithology is 0.40. The concentrations of Ni and Co are both depleted compared to the chondritic values, but Ni is more depleted than Co. The ratios suggest that NWA 11575 has lost a significant amount of metal, as the Ni would partition into the metal at greater rates than the Co.

The magnesium number (Mg#) for the bulk light lithology is 41.3 ±2.1 and for the dark lithology, the Mg# is 44.66 ± 1.44. These values are considered low Mg#'s, suggesting a moderate degree of fractionation, as can be expected with a higher SiO_2 content.

3.0 Discussion

The bulk compositions of the four chemically evolved ungrouped achondrites are plotted in figure 27, a total alkalis vs silica diagram. The similarities in composition between NWA 11575, GRA 06128/9, and Alma-A are apparent, while NWA 11119 is more silica-rich and alkali-poor. NWA 11119, GRA 06128/9, and Alma-A all have ancient crystallization ages, ranging from 4.568 to 4.526 Ga (Srinivasan et al., 2018; Day et al., 2009; Bischoff et al., 2014). The crystallization age of NWA 11575 has not been determined yet, but is expected to be similarly ancient, since melting from radiogenic heating and impacts would have been more likely within the first 1.5-2.5 Ma after the formation of CAIs, and thus more likely to produce significant melting (Sahijpal et al., 2007; Weiss and Elkins-Tanton, 2013). The differences in bulk composition and crystallization ages weakly suggest that igneous processes resulting in evolved compositions were happening on more than one body. The oxygen isotopic compositions of the four silica-rich ungrouped achondrites, which are presented in figure 28, further suggest that these ungrouped achondrites were formed on different bodies. Alma-A and NWA 11119 both have oxygen isotopic compositions that plot within the Ureilite field. GRA 06128/9 plots within the Brachinite field, and NWA 11575 plots within the LL chondrite field. This suggests at least three separate bodies underwent significant heating early in the history of the solar system, which resulted in chemically evolved compositions.

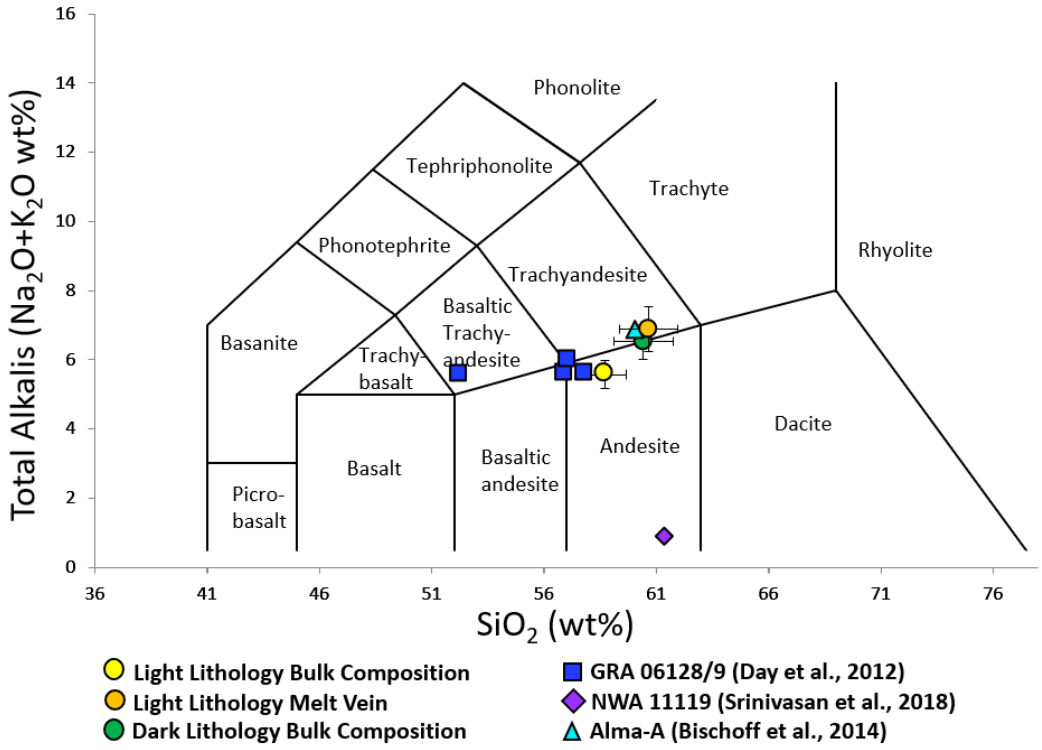

Figure 27. Total alkali vs. silica diagram showing the bulk composition of NWA 11575, GRA 06128/9, NWA 11119, and Alma-A (after Le Bas et al., 1986).

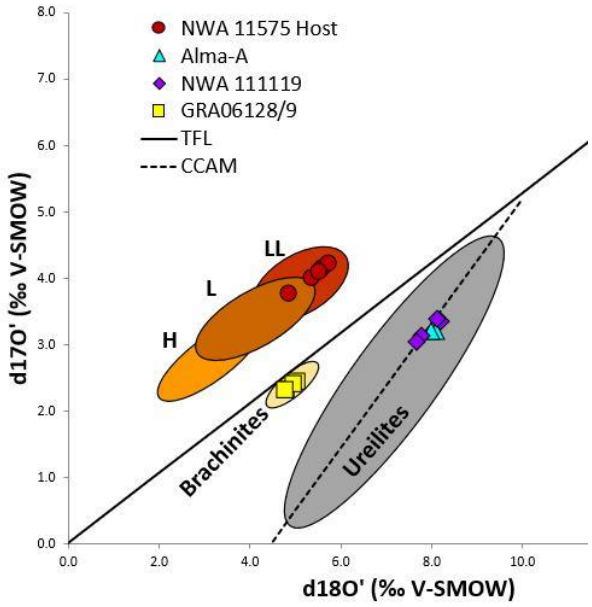

Figure 28. Triple oxygen isotope diagram, showing the distribution in δ17O and δ18O of NWA 11575, GRA 06128/9, Alma-A, and NWA 11119. Data from Day et al. (2009), Srinivasan et al (2018), and Bischoff et al. (2014).

3.1 Pyroxene Compositions

One of the ways in which NWA 11575 is unique from the other silica-rich ungrouped achondrites, is the unusual pyroxene compositional trend. It is similar to lunar samples and martian meteorites, as shown in Figure 29, a series of pyroxene quadrilateral diagrams in which the pyroxenes all have magnesian pigeonite cores, augite mantles, and ferropigeonite rims. Wadhwa et al., (1998) proposed that the trend is a result of first crystallizing the magnesian pigeonite cores, followed by the augite mantles as a result of plagioclase not having begun to crystalize. The composition then shifts to the ferroan pigeonite composition once the plagioclase begins to crystallize. Also noteworthy is that the plots (figure 30) showing TiO_2 wt% versus Al_2O_3 wt% of pigeonite and augite within NWA 11575 and EETA79001B, a martian meteorite with similar pyroxene compositional trends, are remarkably similar. Mikouchi et al. (1999) explain the pyroxene quadrilateral trend and the TiO_2 wt% versus Al_2O_3 wt% trend to be a result of rapid, disequilibrium crystallization from an undercooled magma. The overall lack of exsolution lamellae in the pyroxene crystals is also consistent with a magma that experienced undercooling (Mikouchi et al., 1999).

3.2 Host and Dark Lithology Relationship

The similarities in pyroxene compositions, bulk compositions, Fe/Mn ratios, and oxygen isotopic compositions of the two lithologies strongly suggest that the two lithologies were both derived from the same source and have undergone different cooling and evolution histories. The dark lithology must have formed first, due to the angular, clastic nature of the material embedded within the light lithology, which makes up the bulk of the rock. This suggests that the dark lithology formed earlier and rapidly cooled

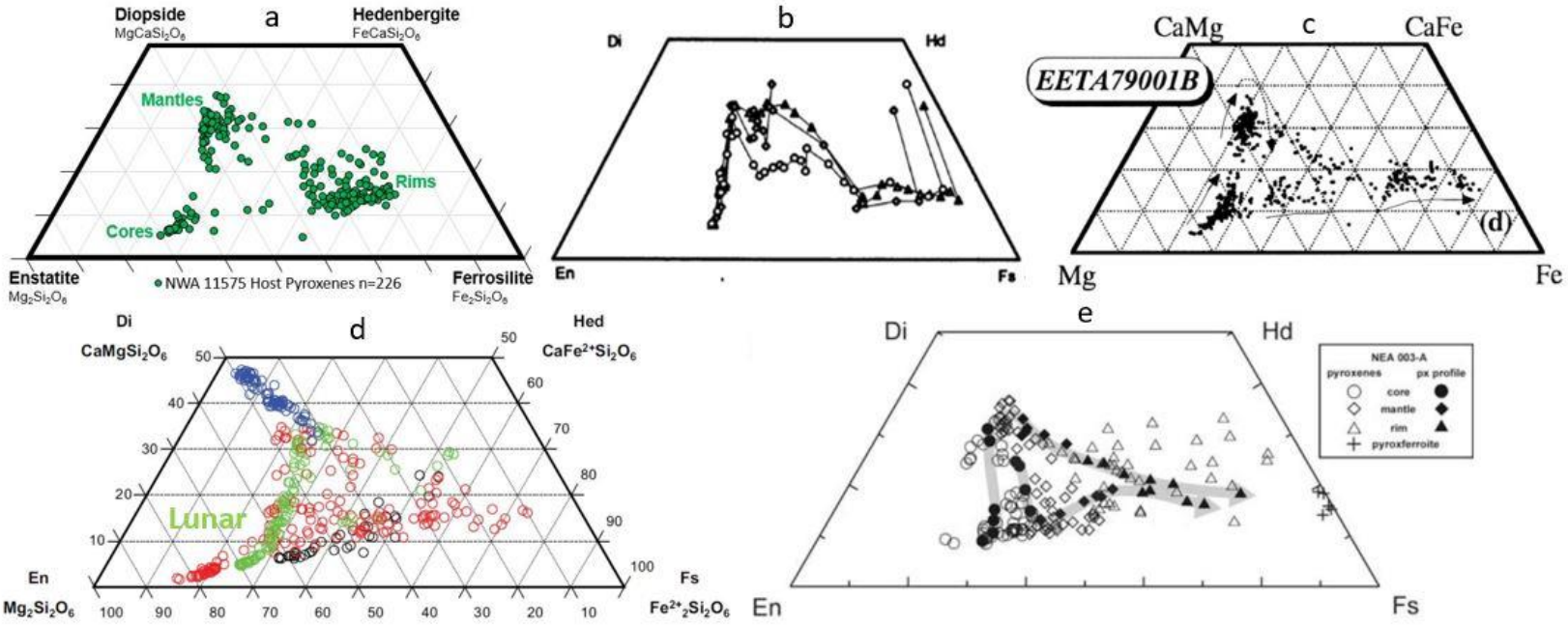

Figure 29. Pyroxene quadrilaterals of NWA 11575 and martian and lunar samples. a) Host lithology of NWA 11575 b) Martian Shergottite Queen Alexandra Range 94201 (QUE 94201) c) Martian meteorite EETA79001B d) Lunar samples 12075, 15499, and 15058, shown in green, and e) Lunar meteorite Northeast Africa 003-A. All show a trend of a magnesian pigeonite core, augite mantle, followed by a ferropigeonite rim. Figures from Karner et al. (2006), Haloda et al. (2009), McKay et al. (1996) and Mikouchi et al (1999).

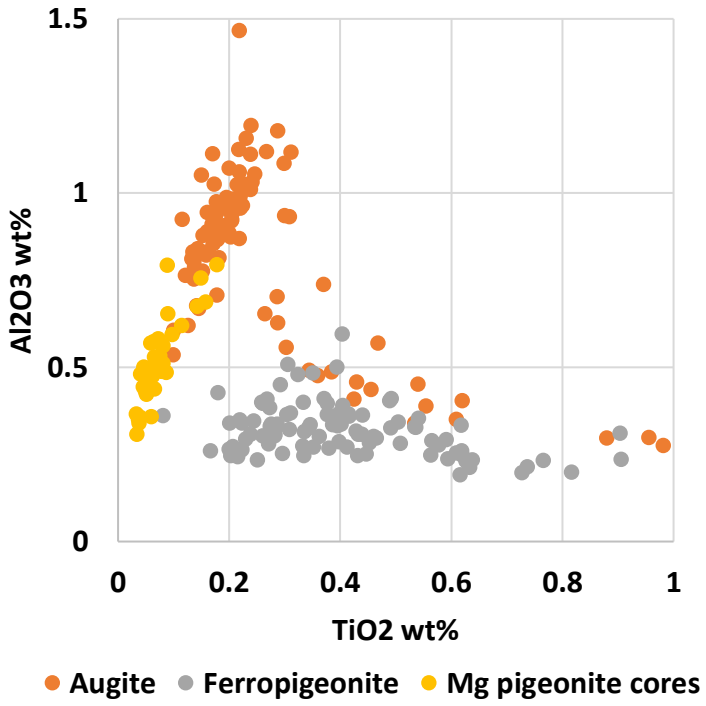

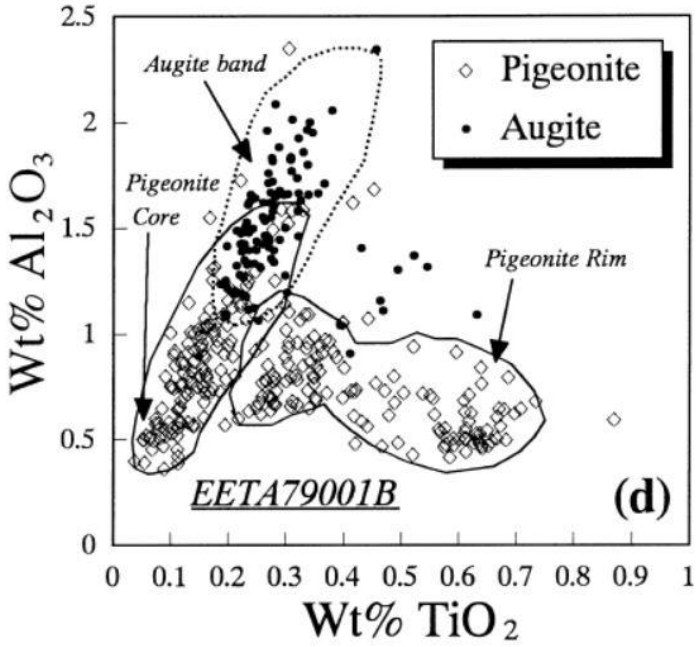

Figure 30. Plots of TiO2 versus Al2O3 in wt% for NWA 11575 (upper) and EETA79001B (lower). The trend is remarkably similar between the two, with the pigeonite core trending towards higher Al2O3 and slightly higher TiO2, followed by the augitic core composition. The ferropigeonite rim drops to a low Al2O3 with varying TiO2 wt%. Figure for EETA79001B from Mikouchi et al., (1999).

to form a lithology consisting largely of a quenched groundmass and euhedral pyroxenes. The dark lithology is likely a chill margin of the same or similar erupted material that crystallized to form the host material. A likely formation sequence begins with the differentiation of a possibly chondritic source to form the evolved trachyandesitic magma. The early erupted material cools quickly on the margins of the flow. As the eruption continues, the fresh magma causes the more brittle, chill margin material to fracture and break up. The chill margin material could easily be fragmented and incorporated into the more recently erupted host material. The timing of these events, which could be determined through crystallization ages is not yet known.

Alternatively, if the magma contained significant volatiles, a more explosive eruption could cause lava to be erupted into the air. This could result in angular, quenched fragments, such as in the dark lithology. The later-erupted material may entrain the dark lithology fragments and cool more slowly.

The final possiblity is that the dark lithology material is simply an impact melt formed from a magma that crystallized and formed a lithology similar in composition to the host lithology. The impact could have melted the prior material, forming the dark lithology material. A later eruption, perhaps spurred by the impact, could have entrained the now quenched impact melt material.

3.3 Possible Origin of NWA 11575

The oxygen, hydrogen, and chromium isotopic compositions of NWA 11575 are similar to those of the LL chondrites. This could suggest a genetic link with ordinary chondrites, or that NWA 11575 formed within the same isotopic reservoir. It's possible

that NWA 11575 could have formed on the LL chondrite parent body, or another similar body within the same isotopic reservoir. This is supported by one-bar partial melting experiments in which Jurewicz et al. (1995) produced an andesitic melt from an LL chondrite, Saint Severin. The resulting composition contained 58 wt% SiO_2, which is similar to the silica content of NWA 11575, 58.70±0.94 wt% SiO_2. Figure 31 illustrates how the removal of olivine via fractional crystallization from an ordinary chondrite bulk composition could result in the bulk composition of NWA 11575. This plot is beneficial in examining how the composition of the melt would change with removal of olivine

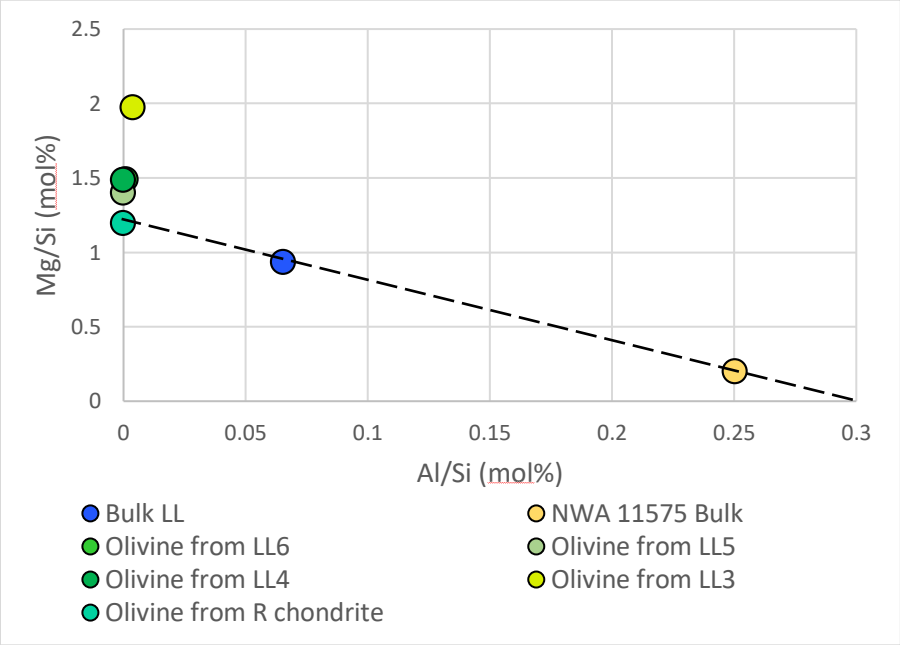

Figure 31. Plot of Al/Si versus Mg/Si modeling the derivation of the bulk composition of NWA 11575 from removal of olivine from an LL chondrite composition. The LL chondrite bulk composition plots in between the bulk composition of NWA 11575 and an olivine composition from an R chondrite, Rumuruti. The three points form a line, suggesting that the removal of olivine would drive the composition towards the bulk composition of NWA 11575. The olivine compositions from LL chondrites of varying petrologic types plot slightly higher on the y-axis. It is important to note, however, that NWA 11575 does not contain any olivine, so the olivine composition that could have been removed from the parent body's bulk composition is not known. Data from Wasson and Kallemeyn (1988), Schulze et al. (1994), McCoy et al. (1990), and Bhandari et al. (2005).

crystals from an LL chondrite-like composition, because Mg, Al, and Si account for the pyroxenes and feldspars, which make up the majority of NWA 11575. Given that NWA 11575 does not contain any olivine, it is also reasonable to consider the removal of olivine as the driving factor for changing the composition of the melt. However, due to the fact that NWA 11575 does not contain any olivine, the composition of the olivine that could have been removed is not known. Thus, it is reasonable to consider multiple olivine compositions, including those included in figure 31, which are olivine compositions from LL chondrites with varying petrologic type and an olivine composition from an R chondrite.

Multiple models exist for the parent body of the LL chondrites, including the single parent body model, models involving multiple parent bodies, and models invoking incremental accretion. The original single parent body model proposed that all the chondrites and achondrites formed on a single parent body approximately the size of a small moon that was partially differentiated, with a metallic core, an igneous silicate layer, and a chondritic crust (Wood, 1958; Weiss & Elkins-Tanton, 2013). However, oxygen isotopes proved the single parent meteorite body model to be invalid, and models involving multiple parent bodies grew in favorability (Clayton et al., 1976; Weiss & Elkins-Tanton, 2013). The oxygen isotopic evidence showed that the different meteorites had isotopic differences that were not possible through isotopic fractionations, but rather reflect formation from different oxygen isotopic reservoirs within a heterogenous solar nebula (Clayton et al., 1976). A variation on the single parent body model is the onion shell model, in which chondrites of varying petrologic types result from internal heating,

with the petrologic type-6 ordinary chondrites located in the interior of the unmelted chondritic parent body (Miyamoto et al., 1981).

Alternatively, the multiple parent body models allow for varying degrees of melting and differentiation on different parent bodies, with unmelted chondritic bodies, partially melted bodies, and fully differentiated bodies. Primitive achondrites, which are partially melted residues that often retain oxygen isotopic signatures or relict chondrules from the parent body, suggest that on some chondritic bodies melting and differentiation occurred to a significant extent (Weisberg et al., 2006; Weiss & Elkins-Tanton, 2013). Additionally, parent bodies could have undergone complete silicate melting, but still retain an unmelted chondritic crust (Anders & Goles, 1961; Weiss & Elkins-Tanton, 2013). Additionally, the body from which NWA 11575 possibly originated could have been fully melted and differentiated, without an unmelted chondritic crust. Figure 32 shows three ideas for the parent body of NWA 11575, based off of an unmelted chondritic model similar to the onion shell model (Miyamoto et al., 1981), the partially differentiated body with a chondritic crust (Elkins-Tanton, 2011; Weiss and Elkins-Tanton, 2013) and a fully melted body (Mason, 1967; Anders & Goles, 1961, Sahijpal et al., 2007; Hevey & Sanders, 2006), but with the addition of one or two magmatic differentiation events that could allow for a silica-rich composition like that of NWA 11575.

Building off of the single parent body model, the chondritic model, presented on the left, consists of an unmelted body similar in composition to LL chondrites, which has been impacted and locally melted. The regions of localized melt would provide a heat source for thermal metamorphism of the underlying crustal material, resulting in

petrologic types 7-3 with a decrease in petrologic type further from the heat source. The regions closest to the melt would have the highest petrologic type, and the regions furthest from the impact melt would remain completely unmelted, with a petrologic type of 3. This model, however, does not account for a method of fractionating or differentiating the magma to produce an evolved, silica-rich composition, such as is evident in NWA 11575.

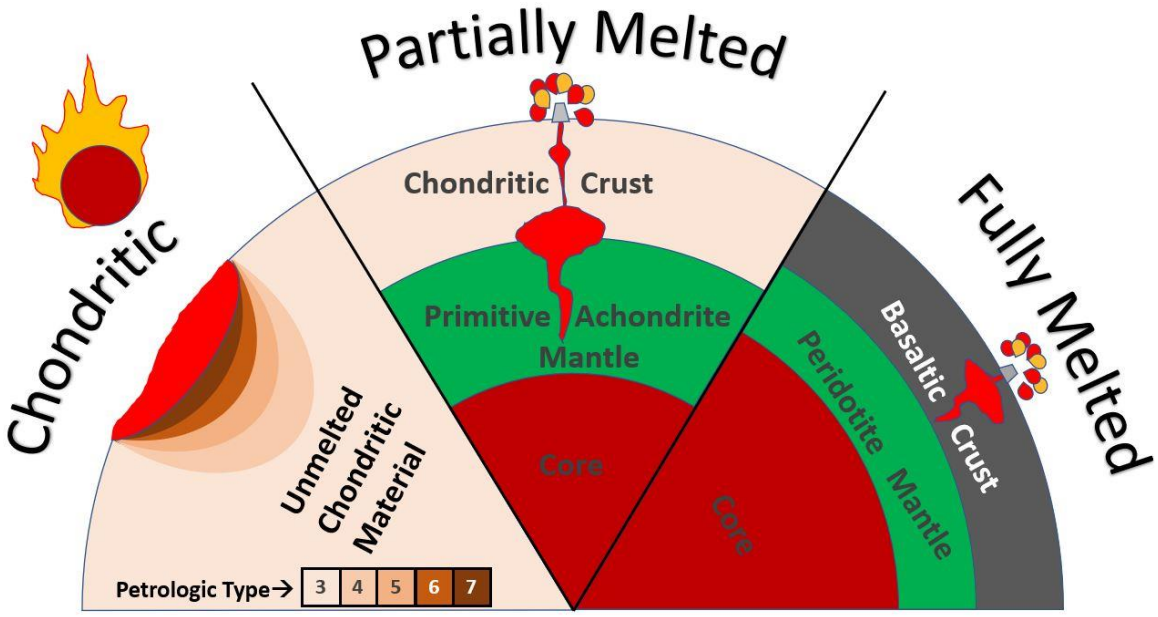

Figure 32 Parent body models for NWA 11575. Three parent body models are displayed in this image. The unmelted, chondritic model is presented on the left, which invokes impact melting as the method of producing a melt from an ordinary chondrite body. In the middle, the partially melted parent body model, modeled after Elkins-Tanton et al. (2013), is presented. The body is internally melted from decay of radiogenic elements. The heat results in a melt that undergoes two differentiation events to reach a silica-rich, andesitic composition. The fully melted parent body model, shown on the right, invokes a body that has been completely melted and differentiated to form a basaltic crust, as suggested by Sahijpal et al., (2007) and Hevey & Sanders (2006). The basaltic crust melts to form an andesitic magma.

The fully melted parent body model, derived from Taylor et al. (1993), McCoy et al. (2006), Sahijpal et al. (2007), Hevey & Sanders (2007), and others, involves the complete melting of a body to form a core, a peridotite mantle, and a basaltic crust. A

fully melted parent body is possible if the body was large (much larger than a 200-400 km diameter body) and able to retain more heat or if the body formed before 1.5 Ma after the formation of CAIs (Hevey & Sanders, 2006). This fits best with the multiple parent body model, in which multiple bodies that formed within the same isotopic reservoir experienced varying degrees of melting and differentiation. Some bodies may have remained completely unmelted, while other bodies experienced full or partial melting during the accretion process. This is necessary to account for the occurrence of LL chondrites, primitive achondrites, and achondrites that retain the LL chondrite isotopic signatures. Because the size of the body on which NWA 11575 formed is not known, this remains a valid possibility for a parent body model for NWA 11575.

The partially melted parent body model has been derived from Weiss & Elkins-Tanton (2013), with the addition of two magmatic differentiation events in order to achieve the silica-rich, andesitic composition of NWA 11575. This is the favored model, because it does not require multiple parent bodies for NWA 11575 and the LL chondrites, and accounts for recent incremental accretion models that predict an unmelted chondritic lid on small bodies. Models that assume instantaneous accretion predict a molten interior and a very thin (~2 km) unmelted crust (Weiss & Elkins-Tanton, 2013; Hevey & Sanders, 2006). Models that invoke incremental accretion allow for a thicker, unmelted crust, but also allow for rapid heating and cooling as the body grows, which slows as the body gains mass (Weiss & Elkins-Tanton, 2013 and references therein). This does provide a problematic scenario for the ascent of magmas through the chondritic crust, however.

A chondritic parent body is expected to have a high-porosity crust, making ascent of magma due to buoyancy difficult. Two possibilities that would allow the magma to

research the surface include either a highly volatile magma or a large impact, which could allow for the ascent of magma through fractures in the crust (Weiss & Elkins-Tanton, 2013). However, a body that forms through incremental accretion would be expected to have a lower volatile content as the volatiles are driven off as water is released (Weiss & Elkins-Tanton, 2013 and references therein). Additionally, it is important to note that these studies are assuming that the magma is basaltic, rather than andesitic, and there is strong evidence that NWA 11575 erupted, i.e. the truncated pyroxene crystals.

Considering the interpretation of the host and dark lithology relationship, there are two possible explanations. The first option is that an erupted magma flows out onto the surface, where the margins of the magma would cool rapidly, particularly on a body with little or no atmosphere. The chill margin material would become brittle and could form what would appear to be angular clasts within the later erupted host lithology. Alternatively, the magma could have erupted in a more explosive manner, and the dark lithology could represent a portion of magma that was erupted more violently and cooled while in the air. In either case, the later-erupted material could cool more slowly if there was more overlying, erupted magma that would act as an insulator for the interior material. This would require either a high volatile content and a thin crust or an impact that would fracture the crust or penetrate into underlying molten material. The vesicles found within the disequilibrium assemblages support NWA 11575 having a high volatile content. Furthermore, the fragmented nature of the pyroxene crystals suggests that mechanical disruption of the crystals occurred before the ferropigeonite layer formed, which was most likely the result of an eruption. This interpretation only requires the body

to have been partially melted, but a body that had been fully melted and differentiated is also possible. An unmelted chondritic layer, such as in the partially melted parent body model, may have been present but simply not sampled in NWA 11575.

4.0 Conclusions

NWA 11575 is an andesitic, ungrouped achondrite consisting of two lithologies. Due to similarities in bulk composition, pyroxene compositional trends, and most importantly, oxygen isotopic compositions, the dark lithology is not a foreign xenolith, but is in fact derived from the same magma. The difference in mineralogy and textures is a result of different cooling rates. The dark lithology must have cooled faster because of the prevalence of the groundmass. The host lithology experienced slow cooling which resulted in the euhedral crystallization of the magnesian pigeonite cores and augitic mantles within the magma chamber. An eruption occurred, causing mechanical disruption of the pyroxene crystals, resulting in pyroxenes with truncated zonation. The eruption also spurred the crystallization of plagioclase and the ferropigeonite rim composition. This petrologic evidence provides strong support that NWA 11575's host lithology was also the result of extrusive volcanism. Due to the low density expected of a chondritic crust, the magma would have either needed to have a lower density than the chondritic crust, have a high volatile content, or require fracturing of the crust via impactors in order to allow for the magma to erupt.

The similarities between NWA 11575 and LL chondrites include oxygen, hydrogen, and chromium isotopic compositions. This suggests a genetic link with LL chondrites. Graphical modeling of the removal of an olivine composition from an LL chondrite bulk composition suggests that this process could result in the bulk composition

of NWA 11575, given a removed olivine composition similar to that of olivine from the R chondrite Rumuruti. Partial melting experiments by Jurewicz et al. (1995) also provide support for the derivation of an andesitic composition from the LL chondrite St. Severin. The model invoking a fully melted silicate portion overlain by a chondritic crust is supported by numerous recent models involving incremental accretion and conduction within the melted interior. The partially melted parent body model provides the simplest explanation for the similarities in isotopic compositions, suggesting that LL chondrites and NWA 11575 could have formed on the same parent body.

NWA 11575 and the other ungrouped achondrites provide evidence for differentiation and chemical evolution on multiple bodies early in the history of the solar system. Oxygen isotopic compositions suggest that at least three different bodies underwent igneous processing, since the isotopic compositions of the various ungrouped achondrites match those of LL chondrites, Brachinites, and Ureilites. Furthermore, NWA 11575 contains pyroxene compositional trends that match those of lunar samples and martian meteorites, which result from significant undercooling of the magma, consistent with eruption. The pyroxene compositional trends and the presence of potassium feldspar and quartz are unique compared with the other silica-rich ungrouped achondrites. Further study of NWA 11575 and the other silica-rich ungrouped achondrites could aid in providing a more complete view of igneous processes in the early solar system.

5.0 Suggestions for Future Work

Age-dating to determine the crystallization age would confirm whether or not NWA 11575 truly is an example of early solar system igneous processes. However, if it

does not have an ancient crystallization age, it could help to constrain a period in which igneous processes were active and evolved compositions were being produced.

Additional experiments using an LL chondrite composition could further support the genetic link between LL chondrites and NWA 11575. The composition produced by Jurewicz et al. (1995) contained a similar SiO_2 wt% content, but further comparison with the mineralogy and textures could provide additional support.

Determination of the density of the melt and modeling the conditions under which the magma ascent could have occurred for the host and dark lithologies could support NWA 11575 being the result of extrusive volcanism, although this is already strongly supported by the mechanically disrupted pyroxene crystals. This could refine the view on the degree and style of melting on parent bodies.

6.0 Methods

6.1 Electron Probe Microanalysis (EPMA)

The JEOL JXA 8200 electron microprobe at the University of New Mexico was used to obtain backscatter electron images, compositional data, and element maps on multiple probe mounts.

Due to the similarity in brightness between the apatite crystals and the pyroxene crystals, the apatite grains were found by tuning the spectrometer to the 197.2 wavelength of phosphorous on a PET crystal (XR2). The beam was slowly rastered over the sample at high-enough magnification to minimize spectrometer defocusing while viewing the resulting X-ray image and BSE image in split-screen mode. The apatite registers as clusters of dots in the x-ray image, which can be matched to the corresponding region in

the compositional view. Qualitative element maps were conducted using EDS or beam mapping on the microprobe, depending on the size of the apatite being measured.

Regarding the microprobe analyses on apatites, a single section of Northwest Africa 11575 was carbon coated and analyzed using a JEOL 8530 field emission electron microprobe at NASA's Johnson Space Center. An accelerating voltage of 15 kV, a nominal probe current of 20 nA, and a beam diameter of 3-5 µm were used during each analysis. Additionally, a ZAF correction was applied to all analyses using the Probe for EPMA software using procedures reported previously in McCubbin et al., (2010). We analyzed the elements Si, Y, Ce, Fe, Mn, Mg, Ca, Na, P, F, Cl, and S. Fluorine was analyzed using a light-element LDE1 detector crystal, and Cl was analyzed using a PET detector crystal. The standards used were as follows: Apatite from SPI Supplies was used as a primary standard for P. Albite from SPI Supplies was used as a primary standard for Na and Si. Ilmenite from the National Museum of Natural History was used as an Fe standard (NMNH 96189; Jarosewich et al., 1980). Apatite from Durango, Mexico, was used as a standard for Ca, and Mn was standardized on rhodonite from SPI supplies. Y was standardized on yttrium orthophosphate, and Ce was standardized on cerium orthophosphate (Jarosewich and Boatner, 1991). Springwater olivine (NMNH 2566) was used as a standard for Mg (Jarosewich et al., 1980). Barite from SPI supplies was used as a primary standard for S. F was standardized on a strontium fluoride standard from JSC. Cl was standardized on tugtupite from SPI supplies, and sodalite was used as a secondary standard for Cl.

In order to reduce or eliminate electron beam damage, we used a 5 µm defocused beam for standardization and 3-5 µm diameter beam for analysis of phosphate grains. Stormer et al. (1993) documented that F and Cl X-ray count rates change with time during

electron microprobe analysis of apatite as a function of crystallographic orientation. Probe for EPMA software was used to monitor for F and Cl X-ray count rate variation in the present study following the procedures of McCubbin et al., (2010). X-ray count rates for F and Cl did not exhibit time-dependent intensity variations over the course of our analyses.

The quality of each phosphate analysis was assessed based on electron microprobe totals and stoichiometric constraints. For apatite, if analytical totals were outside of the range 97.0–102.0 wt.%, the analysis was discarded. If the stoichiometry of the P or Ca sites deviated by more than ±2% (i.e., 0.06 structural formula units (sfu) or 0.10 sfu on a 13 anion basis for the P- and Ca-sites, respectively), the analysis was discarded. Using these constraints, we discarded six of our apatite analyses. For merrillite, if analytical totals were outside of the range 98.0–101.0 wt.%, the analysis was discarded. If the stoichiometry of the P site deviated by more than ±2% (i.e., 0.28 structural formula units (sfu) on a 56 anion basis), the analysis was discarded. Given that merrillite cannot incorporate F or Cl into its structure (McCubbin et al., 2018) and overlap of our beam with apatite was a possibility, we discarded any analyses that had more than 0.1 wt% of either F or Cl. Given that the merrillite can have vacancies on the Ca site, we accepted Ca-site sums between 21 and 22 sfu on a 56 anion basis. Using these constraints, we discarded seven of our merrillite analyses. The quality assessment for apatite and merrillite are similar to those of previous studies on apatite and merrillite in planetary materials (McCubbin et al., 2016; Shearer et al., 2015).

6.2 Scanning Electron Microprobe (SEM)

The JEOL 5800LV Scanning Electron Microscope at the University of New Mexico was used to identify minor phases in NWA 11575, particularly metals, sulfides, and oxides.

6.3 X-ray Diffraction

Small pieces of the host lithology from the SE quadrant of the meteorite were ground to a powder in a mortar and pestle for approximately 10 minutes until the sample had obtained a fine clay-like texture. The powdered sample was placed in a single-crystal quartz holder, which was designed to have a very low background signal, by way of the crystal orientation. The Rigaku SmartLab System at the University of New Mexico was used for the XRD analyses.

6.4 Fiji

The Fiji program was used to determine the percentages of phases in the light and dark lithologies from large mapped or imaged regions. The mapped region in the host lithology measured 3x4 mm. The color threshold tool was used to differentiate between the phases and determine mineralogical percentages. The maps showed complex regions of a silica phase and a k-rich phase in contact with each other. Three such regions were mapped on a smaller scale and the ratios between the silica phase and the potassium feldspar were determined using the threshold function in Fiji. The average of the three ratios was used to refine the quartz and potassium feldspar mineralogical percentages. A weighted average of the pyroxene compositions was used to determine the average pyroxene composition, based on the RGB element maps for the pyroxene crystals. The

bulk composition was calculated from the mineral abundances of major phases, determined using Fiji, along with the average or weighted average (for the zoned pyroxenes) of analyses of each phase within the light lithology.

The Fiji program was also used to determine the bulk composition from a backscatter electron image of a portion of the dark lithology. The threshold tool was used to differentiate between different phases and to give percentages of each phase. The percentages were normalized to 100 to correct for cracks in the sample. This resulted in 70% groundmass and 30% pyroxenes. The bulk composition of the dark lithology was calculated using the average composition of all pyroxenes within the dark lithology and the average composition of the groundmass, along with the data from Fiji.

6.5 Oxygen Isotopes

The MAT 253 mass spectrometer, coupled with an in-situ laser fluorination line, at the Center for Stable Isotopes at the University of New Mexico was used to measure the triple oxygen isotope ratios of the host and dark lithologies. The laser-fluorination line uses a BrF_5 gas in the sample chamber, which reacts with the sample when heated with the CO_2 laser, as described by Sharp (1990). The resulting gases travel through the line until reaching multiple liquid nitrogen traps that cause the unwanted gases to condense onto zeolites within the traps. The remaining oxygen gas is transferred to the MAT 252 mass spectrometer, where the ratios of oxygen-16 to oxygen-17, and oxygen-16 to oxygen-18 are measured relative to the lab standard. The values are presented relative to Vienna Standard Mean Ocean Water (VSMOW).

6.6 NanoSIMS

The Cameca NanoSIMS 50L at NASA's Johnson Space Center was used in multi-collection mode to perform hydrogen isotope analyses of phosphates in a thin section of NWA 11575. A Cs^+ primary ion beam of ~1 nA at the sample was used. The negative secondary ions of ^1H, D, ^{13}C, and ^{18}O were measured concurrently in electron multipliers. The instrument was tuned to achieve a mass resolution of ~3000. The sample and standards were coated with ~10 nm carbon and an electron gun was used; both provided charge compensation.

Prior to analysis, areas of interest approximately 400 μm^2 were pre-sputtered to clean the surface and allow for the identification of the phosphate in the raster area. For each analysis the primary ion beam was rastered over 100 μm^2 areas. Electronic gating was used to restrict counting of secondary ions to the inner 25% of the sputtered area. Each analysis area was divided at 64 x 64 pixels with a 0.54 s dwell time. Each analysis was ~30 minutes long. The highly fractured nature of the phosphate crystals in NWA 11575 meant that cracks sometimes appeared during sputtering. In such cases the signals corresponding to the cracks (high ^1H and ^{13}C counts) were isolated using the NanoSIMS DataEditor software.

Well-characterized reference apatites (c.f. McCubbin et al., 2012) were pressed into indium and were used for correction of measured D/H ratios for instrumental mass fractionation and for calibrating $^1H/^{18}O$ ratios (OH contents) in the unknowns (reported henceforth as H_2O equivalent). A San Carlos olivine crystal also in the indium block was analyzed in the same manner as standards and NWA 11575 and was used to assess instrumental background H_2O. The H_2O background was calculated to be ~70 ppm (n=2)

with a δD of -236 ± 124 ‰ (2SD). A nominally dry crystal in NWA 11575 was also analyzed giving a very similar H_2O content to San Carlos of 65 ppm (n=1) showing that the background calculated on San Carlos is adequate for correcting data in the epoxy mounted thin section. The instrumental background corresponded to <7% total H_2O measured in the unknowns.

6.7 Laser Ablation Inductively Coupled Plasma Mass Spectrometry (LA-ICP-MS)

LA-ICP-MS measurements were performed on an Electro Scientific Instruments New Wave™ UP193FX excimer laser ablation system coupled to a Thermo Element XR™ at the Plasma Analytical Facility, Florida State University. Analytical methods employed followed Yang et al. (2015) and Oulton et al. (2016). Spot analyses were conducted on pyroxene and plagioclase crystals within the host lithology and on pyroxenes and groundmass within the dark lithology. Raster analyses were also conducted to obtain bulk values on both the host and dark lithologies.

6.8 Chromium Isotope Analysis and Inductively Coupled Mass Spectrometry (ICPMS)

A fragment of NWA 11575 (0.08632 g) was crushed using an agate mortar and pestle. The powder was homogenized and then a 0.02436 g aliquot was taken for dissolution. The powder was placed in a PTFE capsule with a 3:1 mixture of concentrated HF:HNO_3 and sealed in a stainless steel Parr jacket. The sealed capsule was heated in an oven at 190°C for 96 hours. The dissolved sample was dried down, treated with concentrated HNO_3 and 6N HCl to break down fluorides formed during the dissolution process. Ninety percent of the dissolved sample was processed for Cr isotope chemistry and 10% remains unprocessed. An aliquot of the 10% remainder was diluted to 3

dilutions (dilution factors of 4435x, 48364x, and 96809x) for trace, minor, and major element determination. A series of dilutions of rock standards (BCR-2 and Allende) were made to generate a calibration curve. A terrestrial USGS rock standard BHVO-2 was also analyzed to compare against literature values to determine accuracy. All samples analyzed (NWA 11575 and BHVO-2 dilutions and calibration curve dilutions) were spiked with a In, Re, Bi solution as an internal standard. The samples were analyzed using a Thermo Element XR high resolution inductively coupled plasma mass spectrometer. Measurements were made in low-, medium-, and high-resolution, depending on potential inferences for a given element. Concentrations were determined by comparison of the signal intensity in the sample, compared to the calibration curve and correcting for dilutions of the original sample solution.

Appendix

Table 1: Representative electron microprobe analyses of pyroxenes and the average and standard deviation for each type of pyroxene analyzed within the host lithology.

	SiO_2	TiO_2	Al_2O_3	Cr_2O_3	FeO	MnO	MgO	CaO	Na_2O	K_2O	Total
Augite	52.51	0.15	0.78	0.86	14.36	0.48	17.61	12.96	0.26	0.02	100.00
Augite	52.32	0.23	1.03	1.04	12.65	0.36	14.46	17.48	0.41	0.01	99.98
Augite	52.48	0.18	0.87	0.83	15.01	0.45	15.94	13.89	0.33	0.02	99.98
Ferroaugite	49.88	0.36	0.48	0.37	28.11	0.63	10.38	9.65	0.20	0.03	100.08
Average	51.53	0.27	0.82	0.76	17.99	0.47	14.18	13.34	0.29	0.02	99.68
SD	1.42	0.19	0.25	0.26	6.36	0.08	3.39	2.24	0.06	0.01	0.38
	SiO_2	TiO_2	Al_2O_3	Cr_2O_3	FeO	MnO	MgO	CaO	Na_2O	K_2O	Total
Ferropigeonite	49.76	0.29	0.45	0.28	31.00	0.71	10.88	6.47	0.15	0.02	100.01
Ferropigeonite	48.75	0.40	0.29	0.22	36.14	0.74	7.35	6.01	0.12	0.00	100.00
Ferropigeonite	49.38	0.31	0.32	0.22	32.60	0.70	9.80	6.52	0.14	0.02	100.01
Ferropigeonite	49.02	0.39	0.36	0.33	33.74	0.68	8.64	6.62	0.17	0.03	99.98
Average	48.88	0.41	0.37	0.24	33.46	0.69	8.94	6.42	0.15	0.03	99.57
SD	0.72	0.16	0.46	0.07	2.29	0.03	1.75	1.04	0.10	0.01	0.42
	SiO_2	TiO_2	Al_2O_3	Cr_2O_3	FeO	MnO	MgO	CaO	Na_2O	K_2O	Total
Mg Pigeonite	53.98	0.07	0.57	0.91	16.30	0.45	24.44	3.17	0.06	0.02	99.98
Mg Pigeonite	53.50	0.09	0.49	0.71	17.29	0.48	23.46	3.88	0.10	0.02	100.01
Mg Pigeonite	53.32	0.05	0.50	0.97	17.24	0.44	24.08	3.28	0.09	0.02	99.98
Mg Pigeonite	53.40	0.07	0.53	0.80	17.78	0.46	23.66	3.18	0.11	0.03	100.03
Average	53.21	0.07	0.52	0.76	17.84	0.49	22.27	4.25	0.12	0.02	99.57
SD	0.68	0.03	0.12	0.16	2.42	0.05	2.46	1.74	0.04	0.01	0.44

Note: Analyses are presented in wt%. SD is the standard deviation of all samples analyzed in that pyroxene type, within the host lithology.

Table 2: Representative electron microprobe analyses of feldspars and the average and standard deviation for each type of feldspar analyzed within the host lithology.

	SiO_2	TiO_2	Al_2O_3	Cr_2O_3	FeO	MnO	MgO	CaO	Na_2O	K_2O	Total
Oligoclase	64.49	0.02	22.38	0.00	0.15	0.00	0.00	2.50	10.16	0.32	100.00
Oligoclase	62.16	0.04	23.75	0.00	0.50	0.01	0.00	4.24	9.10	0.22	100.02
Oligoclase	63.28	0.01	22.76	0.01	0.36	0.00	0.02	3.87	9.33	0.28	99.93
Oligoclase	62.38	0.01	23.49	0.01	0.36	0.01	0.02	4.35	9.10	0.22	99.95
Average	63.45	0.02	23.15	0.00	0.31	0.01	0.01	3.63	9.53	0.24	100.36
SD	0.76	0.01	0.56	0.01	0.10	0.01	0.01	0.47	0.28	0.04	0.45
	SiO_2	TiO_2	Al_2O_3	Cr_2O_3	FeO	MnO	MgO	CaO	Na_2O	K_2O	TOTAL
Orthoclase	64.66	0.05	18.36	0.01	0.18	0.01	0.00	0.04	0.42	16.24	99.98
Orthoclase	64.87	0.08	18.24	0.02	0.18	0.00	0.00	0.07	0.48	16.04	100.03
Orthoclase	64.14	0.08	18.89	0.00	0.20	0.01	0.00	0.04	0.38	16.25	99.99
Orthoclase	64.91	0.05	18.43	0.00	0.24	0.01	0.00	0.04	0.39	15.90	99.98
Orthoclase	63.79	0.07	18.92	0.00	0.20	0.01	0.00	0.03	0.40	16.62	100.04
Orthoclase	71.87	0.13	16.21	0.00	0.51	0.01	0.08	0.14	4.29	7.18	100.42
Average	65.35	0.05	18.06	0.00	0.30	0.01	0.01	0.09	0.72	15.04	99.63
SD	3.93	0.03	1.83	0.01	0.10	0.01	0.02	0.07	0.94	2.93	0.56

Note: Analyses are presented in wt%. SD is the standard deviation of all samples analyzed in that feldspar group, within the host lithology.

Table 3: Representative electron microprobe analyses of apatite and merrillite, and the average and standard deviation, for apatites and merrillites analyzed within the host lithology.

	P_2O_5	SiO_2	Ce_2O_3	Y_2O_3	FeO	MnO	MgO	CaO	Na_2O	F	Cl	SO_3	-O = F + Cl	Total
Apatite	41.97	0.00	0.03	0.00	0.20	0.01	0.00	52.88	0.36	0.00	5.99	0.01	1.35	100.10
Apatite	41.89	0.02	0.00	0.00	0.39	0.02	0.00	53.08	0.34	0.13	5.21	0.01	1.23	99.86
Apatite	42.08	0.00	0.04	0.00	0.25	0.03	0.02	52.87	0.33	0.00	5.73	0.02	1.29	100.09
Apatite	41.53	0.20	0.03	0.00	0.34	0.02	0.11	53.20	0.43	0.13	5.29	0.04	1.25	100.07
Apatite	41.47	0.49	0.05	0.00	0.50	0.03	0.00	52.83	0.22	0.12	5.45	0.04	1.28	99.91
Average	41.54	0.17	0.02	0.00	0.39	0.03	0.02	52.87	0.32	0.03	5.55	0.05	1.27	99.73
SD	0.61	0.25	0.01	0.01	0.22	0.01	0.03	0.76	0.04	0.05	0.27	0.05		
Merrillite	46.35	0.16	0.07	0.06	2.28	0.06	2.68	45.87	2.65	0.00	0.01	0.03	0.00	100.20
Merrillite	45.96	0.38	0.05	0.04	2.29	0.05	2.57	45.38	2.45	0.00	0.02	0.04	0.01	99.23
Merrillite	46.28	0.22	0.06	0.04	2.49	0.06	2.70	45.57	2.64	0.00	0.01	0.02	0.00	100.11
Merrillite	46.65	0.05	0.05	0.07	2.04	0.06	2.63	45.76	2.69	0.00	0.02	0.01	0.00	100.02
Merrillite	46.37	0.00	0.06	0.06	1.98	0.06	2.70	45.92	2.63	0.00	0.01	0.02	0.00	99.80
Average	46.38	0.17	0.06	0.07	2.26	0.06	2.64	45.59	2.64	0.00	0.02	0.02	0.00	99.90
SD	0.40	0.11	0.03	0.07	0.20	0.01	0.05	0.38	0.08	0.00	0.01	0.01		

Note: Analyses are presented in wt%. SD is the standard deviation of all apatite analyzed in the host lithology. bdl indicates concentrations below detection limits.

Table 4: Average and standard deviation of electron microprobe analyses on the groundmass within the dark lithology.

	SiO_2	Al_2O_3	Cr_2O_3	FeO	MnO	MgO	CaO	Na_2O	K_2O	NiO	Total
Average	62.06	15.12	bdl	7.28	0.11	0.70	3.01	8.67	0.22	bdl	97.19
SD	0.94	0.59	bdl	2.21	0.04	0.21	0.97	0.30	0.03	bdl	0.63

Note: Analyses are presented in wt% and bdl indicates concentrations below detection limits.

Table 5: Representative electron microprobe analyses of pyroxenes within the dark lithology, along with the average for each group and the standard deviation.

	SiO_2	TiO_2	Al_2O_3	Cr_2O_3	FeO	MnO	MgO	CaO	Na_2O	K_2O	Total
Augite	51.33	0.38	1.65	0.80	15.69	0.42	13.44	15.79	0.33	0.03	99.87
Augite	50.54	0.54	1.84	0.58	19.75	0.45	10.98	15.03	0.40	0.03	100.14
Augite	51.63	0.30	1.49	1.06	15.30	0.44	15.31	14.20	0.36	0.02	100.11
Average	51.15	0.40	1.90	0.86	16.72	0.44	13.32	14.23	0.54	0.02	99.46
SD	2.14	0.09	2.16	0.36	3.65	0.07	2.65	2.48	1.17	0.03	0.56
	SiO_2	TiO_2	Al_2O_3	Cr_2O_3	FeO	MnO	MgO	CaO	Na_2O	K_2O	Total
Mg Pigeonite	53.78	0.04	0.44	0.75	16.36	0.45	25.20	2.97	0.10	0.03	100.11
Mg Pigeonite	53.93	0.06	0.43	0.74	16.30	0.45	25.08	3.02	0.09	0.03	100.12
Mg Pigeonite	53.60	0.10	0.77	1.03	16.40	0.46	24.56	3.36	0.09	0.01	100.39
Average	53.77	0.14	0.61	0.86	16.95	0.46	22.79	3.92	0.12	0.01	99.53
SD	1.14	0.09	0.29	0.14	1.45	0.03	2.68	2.09	0.06	0.01	0.44

Note: Analyses are presented in wt%

Table 6: Composition data for the shock melt vein within the light lithology.

	SiO_2	Al_2O_3	Cr_2O_3	FeO	MnO	MgO	CaO	Na_2O	K_2O	NiO	TOTAL
Shock Melt Vein	60.65	14.64	0.11	8.69	0.17	2.81	4.86	6.27	0.61	bdl	98.81
SD	1.30	1.63	0.03	1.75	0.04	0.69	0.36	0.47	0.17		0.54

Note: Data is presented in wt% and bdl indicates concentrations below detection limits.

Table 7: Bulk composition data of the host and dark lithologies.

	SiO_2	TiO_2	Al_2O_3	Cr_2O_3	FeO	MnO	MgO	CaO	Na_2O	K_2O	P_2O_5	Total
Host Lithology	58.70	0.06	12.48	0.31	7.04	0.20	7.88	6.55	4.82	0.77	1.17	100.00
SD	0.94	0.05	0.44	0.08	1.64	0.03	1.12	1.05	0.20	0.21	0.00	
Dark Lithology	60.41	0.11	11.31	0.26	10.30	0.21	5.63	5.24	6.36	0.16		100.00
SD	1.32	0.04	0.95	0.09	2.44	0.05	1.75	2.35	0.49	0.03		

Note: Data is presented in wt% and has been calculated according to the methods in section 6.3.

References

Anders, E., and Goles, G.G., 1961, Theories on the Origin of Meteorites: Journal of Chemical Education, v. 38, p. 58-66.

Bhandari, N., Murty, S.V.S., Shukla, P.N., Mahajan, R.R., Shukla, A.D., Suthar, K.M., Parthasarathy, G., and Paliwal, B.S., 2005, Bhawad LL6 chondrite: Chemistry, petrology, noble gases, nuclear tracks, and cosmogenic radionuclides: Meteoritics and Planetary Science, v. 40, p. 1015-1021.

Bischoff, A., Horstmann, M., Barrat, J.-A., Chaussidon, M., Pack, A., Herwartz, D., Ward, D., Vollmer, C., and Decker, S., 2014, Trachyandesitic volcanism in the early Solar System: Proceedings of the National Academy of Sciences of the United States of America, v. 111, p. 12689-12692, doi: 10.1073/pnas.1404799111.

Clayton, R.N., Mayeda, T.K., Goswami, J.N., and Olsen, E.J., 1991, Oxygen isotope studies of ordinary chondrites: Geochimica et Cosmochimica Acta, v. 55, p. 2317-2337.

Clayton, R.N., Onuma, N., Mayeda, T.K., 1976, A classification of meteorites based on oxygen isotopes: Earth and Planetary Science Letters, v. 30, p. 10-18.

Day, J.M.D., Ash, R.D., Liu, Y., Bellucci, J.J., Rumble, D. III, McDonough, W.F., Walker, R.J., and Taylor, L.A., 2009, Early formation of evolved asteroidal crust: Nature Letters, v. 457, p. 179-182, doi:10.1038/nature07651.

Day, J.M.D., Walker, R.J., Ash, R.D., Liu, Y., Rumble III, D., Irving, A.J., Goodrich, C.A., Tait, K., McDonough, W.F., and Taylor, L.A., 2012, Origin of felsic achondrites Graves Nunataks 06128 and 06129, and ultramafic brachinites and brachinite-like achondrites by partial melting of volatile-rich primitive parent bodies: Geochimica et Cosmochimica Acta, v. 81, p. 94-128.

Droop, G.T.R., 1987, A general equation for estimating Fe3+ concentrations in ferromagnesian silicates and oxides from microprobe analyses, using stoichiometric criteria: Mineralogical Magazine, v. 51, p. 431-5.

Elkins-Tanton, L.T., Weiss, B.P., and Zuber, M.T., 2011, Chondrites as samples of differentiated planetesimals: Earth and Planetary Science Letters, v. 305, p. 1-10.

Hallis, L.J., 2016, D/H ratios of the inner Solar System, Philosophical Transactions Royal Society A, v. 375, p. 1-17.

Haloda, J., Týcová, P., Korotev, R.L., Fernandes, V.A., Burgess, R., Thöni, M., Jelenc, M., Jakeš, P., Gabzdyl, P., and Košler, J., 2009, Petrology, geochemistry, and age of low-Ti mare-basalt meteorite Northeast Africa 003-A: A possible member of the Apollo 15 mare basaltic suite: Geochimica et Cosmochimica Acta, v. 73, p. 3450-3470, doi:10.1016/j.gca.2009.03.003.

Hevey, P.J. and Sanders, I.S., 2006, A model for planetesimal meltdown by ^{26}Al and its implications for meteorite parent bodies: Meteoritics and Planetary Science, v. 41, p. 95-106.

Hovis, G.L. and Harlov, D.E., 2010, Solution calorimetric investigation of fluor-chlorapatite crystalline solutions: American Mineralogist, v. 95, p. 946-952.

Jarosewich, E. and Boatner, L.A., 1991, Rare-earth element reference samples for electron-microprobe analysis: Geostandards Newsletter, v. 15, p. 397-399.

Jarosewich, E., Nelen, J.A. and Norberg, J.A., 1980, Reference samples for electron microprobe analysis: Geostandards Newsletter, v. 4, p. 43-47.

Jones, R.H., McCubbin, F.M., Dreeland, L., Guan, Y.B., Burger, P.V., and Shearer, C.K., 2014, Phosphate minerals in LL chondrites: A record of the action of fluids during metamorphism on ordinary chondrite parent bodies: Geochimica et Cosmochimica Acta, v. 132, p. 120-140.

Jones, R.H., McCubbin, F.M., and Guan, Y., 2016, Phosphate minerals in the H group of ordinary chondrites, and fluid activity recorded by apatite heterogeneity in the Zag H3-6 regolith breccia: American Mineralogist, v. 101, p. 2452-2467.

Jurewicz, A.J.G., Mittlefehldt, D.W., and Jones, J.H., 1995, Experimental partial melting of the St. Severin (LL) and Lost City (H) chondrites: Geochimica at Cosmochimica Acta, v. 59, p. 391-408.

Karner, J., Papike, J.J., and Shearer, C. K., 2006, Comparative planetary mineralogy: Pyroxene major- and minor-element chemistry and partitioning of vanadium between pyroxene and melt in planetary basalts: American Mineralogist, v. 91, p. 1574-1582, doi: 0.2138/am.2006.2103.

Le Bas, M.J., Le Maitre, R.W., Streckeisen, A., and Zanettin, B., 1986, A Chemical Classification of Volcanic Rocks Based on the Total Alkali-Silica Diagram: Journal of Petrology, v. 27, p. 745-750.

Lewis, J.A. and Jones, R.H., 2016, Phosphate and feldspar mineralogy of equilibrated L chondrites: The record of metasomatism during metamorphism in ordinary chondrite parent bodies: Meteoritics & Planetary Science, v. 51, p. 1886-1913, doi: 10.1111/maps.12719.

Lodders, K., 2003, Solar system abundances and condensation temperatures of the elements: The Astrophysical Journal, v. 591, p. 1220-1247.

Mahaffy, P.R., Donahue, T.M., Atreya, S.K., Owen, T.C., and Niemann, H.B., 1998, Galileo Probe measurements of D/H and $^{3}He/^{4}He$ in Jupiter's Atmosphere: Space Science Reviews, v. 84, p. 251-263.

Mason, B., 1967, Meteorites: American Scientist, v. 55, p. 429-455.

McCoy T. J., Mittlefehldt D. W., and Wilson L., 2006, Asteroid differentiation *in* Lauretta, D.S., and McSween, H.Y., ed., Meteorites and the Early Solar System II, Tucson, AZ, p. 733-746.

McCoy, T.J., Scott, E.R.D., Jones, R.H., Keil, K., and Taylor, G.J., 1990, Composition of chondrule silicates in LL3-5 chondrites and implications for their nebular history and parent body metamorphism: Geochimica et Cosmochimica Acta, v. 55, p. 601-619.

McCubbin, F.M., and Ustunisik, G., 2018, Experimental investigation of F and Cl partitioning between apatite and Fe-rich basaltic melt at 0 GPa and 950-1050 °C: Evidence for steric controls on apatite-melt exchange equilibria in OH-poor apatite: American Mineralogist, v. 103, p. 1455-1467.

McCubbin, F.M., Boyce, J.W., Srinivasan, P., Santos, A.R., Elardo, S.M., Filiberto, J., Steele, A., and Shearer, C.K., 2016, Heterogeneous distribution of H_2O in the martian interior: Implications for the abundance of H_2O in depleted and enriched mantle sources: Meteoritics & Planetary Science, v. 51, p. 2036-2060.

McCubbin, F.M., Hauri, E.H., Elardo, S.M., Vander Kaaden, K.E., Wang, J., and Shearer, C.K., 2012, Hydrous melting of the martian mantle produced both depleted and enriched shergottites: Geology, v. 40, p. 683-686.

McCubbin, F.M., Shearer, C.K., Burger, P.V., Hauri, E.H., Wang, J.H., Elardo, S.M., and Papike, J.J., 2014, Volatile abundances of coexisting merrillite and apatite in the martian meteorite Shergotty: Implications for merrillite in hydrous magmas: American Mineralogist, v. 99, p. 1347-1354.

McCubbin, F.M., Steele, A., Nekvasil, H., Schnieders, A., Rose, T., Fries, M., Carpenter, P.K. and Jolliff, B.L., 2010, Detection of structurally bound hydroxyl in fluorapatite from Apollo mare basalt 15058,128 using TOF-SIMS: American Mineralogist v. 95, p. 1141-1150.

McCubbin, F.M., Phillips, B.L., Adcock, C.T., Tait, K.T., Steele, A., Vaughn, J.S., Fries, M.D., Atudorei, V., Vander Kaaden, K.E., and Hausrath, E.M., 2018, Discreditation of bobdownsite and the establishment of criteria for the identification of minerals with essential monofluorophosphate (PO_3F^{2-}): American Mineralogist, v. 103, p. 1319-1328.

McKay, G., Yang, S.-R., and Wagstaff, J., 1996, Complex zoned pyroxenes in shergottite QUE 94201: Evidence for a two-stage crystallization history: Lunar and Planetary Science XXVII, abstract 852.

McLeod, C.L., and Krekeler, M.P.S., 2017, Sources of Extraterrestrial Rare Earth Elements: To the Moon and Beyond: Resources, v. 6, p. 1-28, doi: 10.3390/resources6030040.

Mikouchi, T., Miyamoto, M., and McKay, G.A., 1999, The role of undercooling in producing igneous zoning trends in pyroxenes and maskelynites among basaltic Martian meteorites: Earth and Planetary Science Letters, v. 173, p. 235-356.

Miyamoto, M., Fujii, N., and Takeda, H., 1981, Ordinary chondrite parent body: An internal heating model: Proceedings of Planetary Science, v. 12B, p. 1145-1152.

Oulton, J., Humayun, M., Fedkin, A., and Grossman, L., 2016, Chemical evidence for differentiation, evaporation, and recondensation from silicate clasts in Gujba: Geochimica et Cosmochimica Acta, v. 177, p. 254-274.

Papike, J.J., Karner, J.M., Shearer, C.K., and Burgerm P.V., 2009, Silicate mineralogy of martian meteorites: Geochimica et Cosmochimica Acta, v. 73, p. 7443-7485, doi: 10.1016/j.gca.2009.09.008.

Righter, K., Drake, M.J., and Scott, E., 2006, Compositional Relationships Between Meteorites and Terrestrial Planets *in* Lauretta, D.S., and McSween, H.Y., ed., Meteorites and the Early Solar System II, Tucson, AZ, p. 803-828.

Robert, F., Gautier, D., and Dubrulle, B., 2000, The solar system D/H ratio: Observations and Theories: Space Science Reviews, v. 92, p. 201-224.

Sahijpal, S., Soni, P., and Gupta, G., 2007, Numerical simulations of the differentiation of accreting planetesimals with ^{26}Al and ^{60}Fe as the heat sources: Meteoritics and Planetary Science, v. 42, p. 1529-1548.

Schettler, G., Gottschalk, M., and Harlov, D.E., 2011, A new semi-micro wet chemical method for apatite analysis and its application to the crystal chemistry of fluorapatite-chlorapatite solid solutions: American Mineralogist, v. 96, p. 138-152.

Schulze, H., Bischoff, A., Palme, H., Spettel, B., Dreibus, G., and Otto, J., 1994, Mineralogy and chemistry of Rumuruti: The first meteorite fall of the new R chondrite group: Meteoritics and Planetary Science, v. 29, p. 275-286.

Sharp, Z., 2017, Nebular ingassing as a source of volatiles to the Terrestrial planets: Chemical Geology, v. 448, p. 137-150.

Sharp, Z., 2018, Extraterrestrial Materials, *in* Principles of Stable Isotope Geochemistry, p. 350-379.

Sharp, Z., 1990, A laser-based microanalytical method for the in situ determination of oxygen isotope ratios of silicates and oxides: Geochimica et Cosmochimica Acta, v. 54, p. 1353-1357, doi: 10.1016/0016-7037(90)90160-M.

Shearer, C.K., Burger, P.V., Neal, C., Sharp, Z., Spivak-Birndorf, L., Borg, L., Fernandes, V.A., Papike, J.J., Karner, J., Wadhwa, M., Gaffney, A., Shafer, J., Geissman, J., Atudorei, N.-V., Herd, C., Weiss, B.P., King, P.L., Crowther, S.A., and Gilmour, J.D., 2010, Non-baslatic asteroidal magmatism during the earliest stages of solar system evolution: A view from Antarctic achondrites Graves Nunatak 06128 and 06129: Geochimica et Cosmochimica Acta, v. 74, p. 1173-1199.

Shearer, C.K., Burger, P.V., Papike, J.J., McCubbin, F.M., and Bell, A.S., 2015, Crystal chemistry of merrillite from Martian meteorites: Mineralogical recorders of magmatic processes and planetary differentiation: Meteoritics & Planetary Science, v. 50, p. 649-673.

Shearer, C.K., Burger, P.V., Papike, J.J., Sharp, Z.D., and McKeegan, K.D., 2011, Fluids on differentiated asteroids: Evidence from phosphates in differentiated meteorites GRA 06128 and GRA 06129: Meteoritics & Planetary Science, v. 46, p. 1345-1362, doi: 10.1111/j.1945-5100.2011.01233.x.

Srinivasan, P., Dunlap, D.R., Agee, C.B., Wadhwa, M., Coleff, D., Ziegler, K., Zeigler, R., and McCubbin, F.M., 2018, Silica-rich volcanism in the early solar system dated at 4.565 Ga: Nature Communications, v. 9, p. 1-8, doi: 10.1038/s41467-018-05501-0.

Stormer, J.C., Pierson, M.L. and Tacker, R.C., 1993, Variation of F-X-ray and Cl-X-ray intensity due to anisotropic diffusion in apatite during electron-microprobe analysis: American Mineralogist, v. 78, p. 641-648.

Taylor, J.G., Keil, K., McCoy, T., Haack, H., and Scott, E.R.D., 1993, Asteroid Differentiation: Pyroclastic Volcanism to Magma Oceans: Meteoritics, v. 28, p. 34-52.

Wadhwa, M., Crozaz, G., Taylor, L.A, and McSween, H.Y., 1998, Martian basalt (shergottite) Queen Alexandra Range 94201 and lunar basalt 15555: A tale of two pyroxenes: Meteoritics and Planetary Science, v. 33, p. 321-328.

Warren, P.H., 2011a, Stable isotopes and the noncarbonaceous derivation of ureilites, in common with nearly all differentiated planetary materials: Geochimica et Cosmochimica Acta, v. 75, p. 6912-6926, doi: 10.1016/j.gca.2011.09.011.

Warren, P.H., 2011b, Stable isotopic anomalies and the accretionary assemblage of the Earth and Mars: A subordinate role for the carbonaceous chondrites: Earth and Planetary Science Letters, v. 311, p. 93-100, doi: 10.1016/j.epsl.2011.08.047.

Wasson, T.J., and Kallemeyn, G.W., 1988, Composition of chondrites: Philosophical Transactions of the Royal Society, v. 325, p. 535-544, doi: 10.1098/rsta.1988.0066.

Weisberg, M.K., McCoy, T.J., and Krot, A.N., 2006, Systematics and Evaluation of Meteorite Classification *in* Lauretta, D.S., and McSween, H.Y., ed., Meteorites and the Early Solar System II, Tucson, AZ, p. 19-52.

Weiss, B.P., and Elkins-Tanton, L.T., 2013, Differentiated Planetesimals and the Parent Bodies of Chondrites: Annual Review of Earth and Planetary Sciences, v. 41, p. 529-560, doi: 10.1146/annurev-earth-040610-1335.

Wood, J.A., 1958, Silicate Meteorite Structures and the Origin of the Meteorites: PhD Thesis, Massachusetts Institute of Technology.

Yang, S., Humayun, M., Righter, K., Jefferson, G., Fields, D., and Irving, A.J., 2015, Siderophile and chalcophile element abundances in shergottites: Implications for Martian core formation: Meteoritics and Planetary Science, v. 50, p. 691-714.